

Turbulence-driven thermal and kinetic energy fluxes in the atmospheres of hot Jupiters

Taeho Ryu^{1*}, Michael Zingale¹, Rosalba Perna¹

¹*Department of Physics and Astronomy, Stony Brook University, Stony Brook, NY 11794-3800, USA*

Accepted XXX. Received YYY; in original form ZZZ

ABSTRACT

We have performed high resolution 3–dimensional compressible hydrodynamics simulations to investigate the effects of shocks and turbulence on energy transport into hot Jupiter atmospheres, under a variety of shear gradients. We focus on a local atmospheric region to accurately follow the small-scale structures of turbulence and shocks. We find that the effects of turbulence above and below a shear layer are different in scale and magnitude: below the shear layer, the effects of turbulence on the vertical energy transfer are local, generally $\lesssim 2 \times$ (scale height). However, turbulence can have a spatially and thermally-large influence on almost the entire region above the shear layer. We also find that shock formation is local and transient. Once the atmosphere becomes steady, the time-averaged heat flux at $P \sim 1$ bar is insignificant, on the order of 0.001% of the incoming stellar flux with a shear motion at $P \simeq 1$ mbar, and 0.1% with a deeper shear layer at $P \simeq 100$ mbar. Accordingly, the diffusion coefficient is higher for the deeper shear layer. Therefore, our results suggest that turbulence near less dense ($P \simeq 1$ mbar) regions does not cause a sufficiently deep and large penetration of thermal energy to account for radius inflation in hot Jupiters, regardless of how violent the turbulence is. However, as the shear layer gets deeper, heat transfer becomes more effective throughout the atmosphere (upwards and downwards) due to a larger kinetic energy budget. Therefore, it is more important how deep turbulence occurs in the atmosphere, than how unstable the atmosphere is for effective energy transfer.

Key words: Hot Jupiter – planetary systems : atmosphere – planetary systems : gaseous planet

1 INTRODUCTION

Hot Jupiters are a class of gas-giant exoplanets, characterized by short orbital periods ($P \lesssim 50$ days). Such close proximity to their parent stars leads to several interesting features, which include tidal synchronization, strong irradiation, and a generally large day-night temperature contrast. A number of hot Jupiters are observed to have radii larger than what predicted from standard cooling models (e.g. Showman & Guillot 2002; Guillot & Showman 2002; Howard et al. 2012; Wang et al. 2015). The origin of the radius inflation is still debated, and several ideas have been put forward to explain it.

Inflated radii imply that the bloated planets retain more internal entropy than expected. This could be produced by either injection/dissipation of heat, or less efficient energy loss, or a combination of both. Within this context, the mechanisms that have been put forward to explain the radius

anomaly can be divided into two classes. The first category includes less efficient cooling due to enhanced opacity (Burrows et al. 2007). As the opacity increases, cooling becomes inefficient and the planets can naturally retain more internal heat. The second category invokes extra heat sources in the interior, such as the dissipation of heat via tidal forces (Bodenheimer et al. 2001; Jackson et al. 2008; Ibgui & Burrows 2009; Ibgui et al. 2011), conversion of the stellar flux into kinetic energy of the global atmospheric flow, driven by the large day-night temperature gradient (often called “hydrodynamic dissipation”; Showman & Guillot 2002; Guillot & Showman 2002; Showman et al. 2009; Heng et al. 2011a,b), magnetic drag in ionized planetary winds, or “ohmic dissipation” (Batygin & Stevenson 2010; Perna et al. 2010a,b, 2012), and dissipation of energy induced by fluid instabilities (Li & Goodman 2010). For a comprehensive comparison and review, see Heng & Showman (2015).

Among those, energy dissipation via turbulence (Li & Goodman 2010), likely accompanied by shocks (Perna et al.

* email: taeho.ryu@stonybrook.edu

2012; Dobbs-Dixon & Agol 2013; Heng 2012)¹, could be a viable, or at least interesting mechanism to consider. This is because turbulence may be ubiquitous and present even in stably stratified atmospheres. It is hence natural to study its onset in globally circulating planetary atmospheres. Youdin & Mitchell (2010) proposed that forced turbulence can drive downward transport of heat in the outer radiative zone of stratified atmospheres. They called this the “mechanical greenhouse effect”², and built an analytic model of the outer radiative zone, focusing on diffusion and dissipation by forced turbulence. They found that a heat flux generated by forced turbulence propagates downwards and can be deposited in deeper regions. Their analytic approach, undoubtedly necessary for understanding the underlying physics, is however more suitable for somewhat idealized cases. To account for a more realistic scenario, simulations with detailed modelling are essential. Recently, using the compressible shock-capturing code RAMSES, Fromang et al. (2016) developed a 3-dimensional model to examine the role of shear-driven instabilities and shocks in planetary atmospheres, using a Newtonian relaxation scheme. They covered a large volume of the atmosphere to take into account global motions and included cooling via a Newtonian cooling method. Their simulations suggest that equatorial jets are subject to shear-driven instabilities, which can lead to a sufficiently large amount of downward kinetic energy flux and the formation of shocks at a few mbar pressure levels. Their results improve and deepen our understanding of the physics of turbulence and shocks. However, as they pointed out in their paper, it is possible that their spatial resolution may still be too large to capture processes occurring on small scales.

Motivated by those studies and in order to improve on some of their limitations, in this work we investigate the effect of shocks and turbulence on energy penetration in stable stratified atmospheres, using high resolution 3-dimensional compressible hydrodynamics simulations with the adaptive-mesh finite-volume code CASTRO (Almgren et al. 2010). We focus on a local atmospheric region to accurately capture the small-scale structures of the eddy motion. We estimate how much and how deep heat can be deposited in the atmosphere when shear motions are driven. Based on the measured heat flux, we further estimate the diffusion coefficient K_{zz} (see Equation 14). Last, we discuss the formation, duration and distribution of shocks in the planetary atmospheres.

In our suites of simulations, we find that the effects of turbulence on the kinetic and heat energy transfer are local, generally confined to within a spatial range of $z \sim 2H$ (where H is the scale height) below where eddies are created, but turbulence can make a spatially and thermally large-scale impact on the regions above it. We also find that shock formation is local and transient. The time-averaged heat energy flux at $P \sim 1$ bar when the atmosphere becomes steady is on the order of 0.1 – 001% of the incoming stellar flux depending on the location of the shear layer (lower flux for

an outer shear layer). Hence, our results suggest that turbulence near less dense regions ($P \gtrsim 1$ mbar) does not lead to a sufficient amount of thermal energy burial in deeper regions to account for the inflated radii of hot Jupiters, regardless of how violent the turbulence is. On the other hand, thermal energy can be transferred more effectively throughout the atmosphere when turbulence is triggered at deeper regions ($P \gtrsim 100$ mbar). Therefore, it is more important how deep turbulence occurs in the atmosphere, than how unstable the atmosphere is for effective transfer of energy.

This paper is organized as follows. In Section 2, we explain our numerical setup including the model description (Section 2.1) and the boundary conditions (Section 2.2), and describe our shear prescription (Section 2.3) and initial model parameters (Section 2.4). We present our results in Section 3. In Section 4, we first compare our results with two different numerical resolutions for the same set-up, and then we compare simulations at higher resolution but with different atmospheric depths for the shear layer. Finally, we conclude with a summary of our findings in Section 7.

2 NUMERICAL SETUP

In this section we present our planetary atmosphere models. We describe the initial conditions of the model atmospheres and our shear prescription.

2.1 Model description

In order to follow the evolution of our model atmosphere, we solve the 3-dimensional hydrodynamic equations in a Cartesian coordinate system, using the code CASTRO (Almgren et al. 2010). CASTRO is an adaptive mesh, compressible radiation-hydrodynamics simulation code, based on an Eulerian grid. It supports a general equation of state, nuclear reaction networks, rotation, and full self-gravity. The fully compressible equations computed in the code CASTRO are as follows,

$$\frac{\partial \rho}{\partial t} = -\nabla \cdot (\rho \mathbf{u}), \quad (1)$$

$$\frac{\partial (\rho \mathbf{u})}{\partial t} = \nabla \cdot (\rho \mathbf{u} \mathbf{u}) - \nabla P + \rho \mathbf{g} + \mathbf{S}_{\text{src}}, \quad (2)$$

$$\frac{\partial (\rho E)}{\partial t} = -\nabla \cdot (\rho \mathbf{u} E + P \mathbf{u}) + \rho \mathbf{u} \cdot \mathbf{g} + \mathbf{u} \cdot \mathbf{S}_{\text{src}}, \quad (3)$$

where ρ , \mathbf{u} , and P are the density, velocity vector, and pressure, respectively. E represents the total specific energy, given by the sum of the internal energy e and the kinetic energy, i.e., $E = e + \mathbf{u} \cdot \mathbf{u}/2$. \mathbf{S}_{src} is a user-specified momentum source term, which will be described in more detail in §2.3. CASTRO is suitable for capturing small scale structures of turbulence, which is our primary goal in this study.

We consider a three-dimensional computational domain with the shape of a rectangular prism (the height is twice the width). In our simulations, we model the radiative region of strongly-irradiated planets assuming it is initially in hydrostatic equilibrium with a constant gravity $g = 10^3 \text{ cm s}^{-2}$. We fill the domain with our model atmosphere, starting at the bottom at $P \simeq 10$ bar, and approaching the top so that

¹ Generally, fluid in a stably stratified atmosphere becomes unstable when the shear stress, or velocity gradient, is sufficiently large that buoyancy forces suppress the vertical displacements of fluid elements. Therefore, high-speed flows are more likely subject to the instability.

² See Izakov (2001) for the greenhouse effect in the atmosphere of Venus.

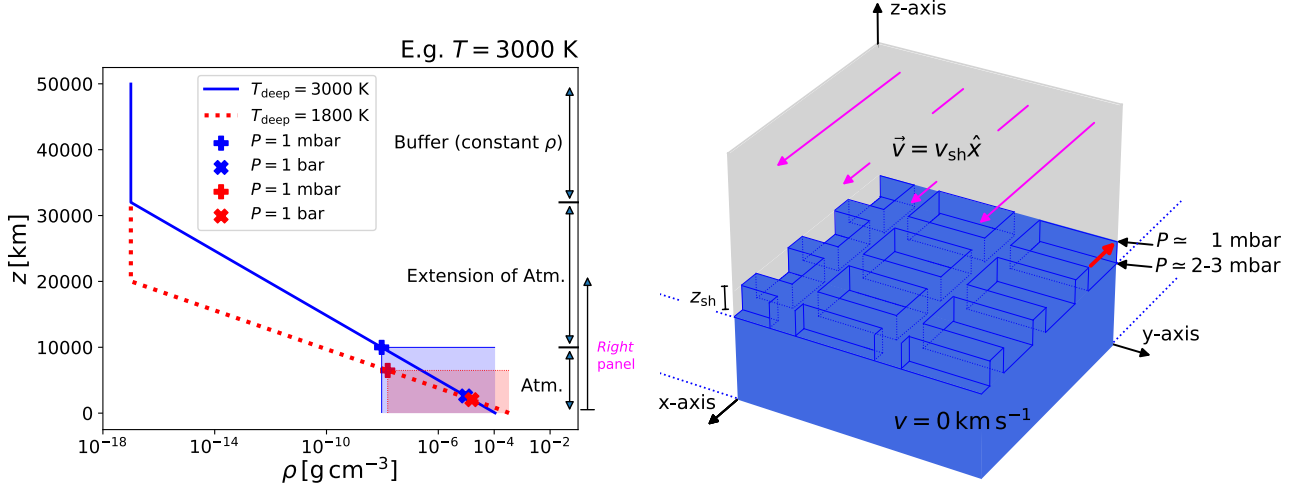


Figure 1. *Left panel:* The $\rho - z$ plot for $T = 1800$ K and 3000 K. The shaded regions on the bottom-right corner indicate the atmospheres with $P \geq 1$ mbar. In particular, the annotations near the right vertical axis (i.e. Buffer, Extension of Atm. and Atm.) refer to the case $T = 3000$ K. Furthermore, the arrow outside the same vertical axis, annotated with "Right panel" in magenta, roughly shows the spatial scale of the schematic diagram of the atmosphere in our computation box, which is shown in the *right panel*. *Right panel:* Schematic diagram of one corner of the computation box for our fiducial model. The blue region indicates our model atmosphere with initially $v = 0$ km s $^{-1}$. On top of it, the gas is given a shear velocity $v = v_{\text{sh}}$ in the x direction, indicated with magenta arrows. A shear layer in between, extending from $P = 1$ mbar to $P \approx 2 - 3$ mbar, has a positive vertical gradient of v_x . Notice that the relative size of the corrugations shown in this plot is exaggerated for visualization.

Table 1. Model parameters considered in this study. We categorize the parameters into two groups: model parameters that all models share, and those which differ among models. From left to right: The common parameters include the number of cells N_{cell} , the number of cells per scale height $H/\Delta l$ (H : scale height), the gravitational constant g [cm s $^{-2}$], and the shear velocity in units of the Mach number \mathcal{M}_{sh} . In the category of the different parameters, we list the size of our computation box L [10^4 km], the height $z_{P=1 \text{ mbar}}$ [10^4 km] at $P = 1$ mbar, the initial T in the radiative zone T_{deep} [K], P at the radiative-convective boundary P_{RCB} [bar], P at the bottom of the domain $P_{z=0}$ [bar], the Richardson number Ri , estimated at $t = 0$ and the sound speed c_s [km s $^{-1}$].

Model name	same model parameters				different model parameters						
	$N_{\text{cell}} = (N_x, N_y, N_z)$	$H/\Delta l$	g	\mathcal{M}_{sh}	(L_x, L_y, L_z)	$z_{P=1 \text{ mbar}}$	T_{deep}	P_{RCB}	$P_{z=0}$	$Ri(t=0)$	c_s
$T3000 - Ri0.02$	(512, 512, 1024)	20	10^3	1	(2.5, 2.5, 5.0)	1.00	3000	268	12	0.02	3.86
$T3000 - Ri0.1$										0.1	
$T3000 - Ri0.25$										0.25	
$T1800 - Ri0.02$										0.02	
$T1800 - Ri0.1$										0.1	
$T1800 - Ri0.25$										0.25	

The same six models above, but with a lower resolution $N_{\text{cell}} = (256, 256, 512)$

the atmosphere at a level of $P \approx 1$ mbar occupies around 20% of the entire domain. We define $P = 1$ mbar as the top of the atmospheres in this study. Then, we further extend the atmosphere until the density becomes smaller than $\rho = 10^{-17}$ g cm $^{-3}$ ($\sim 44\%$ of the domain). We fill the rest of the domain ($\sim 36\%$) with a constant density medium with $\rho = 10^{-17}$ g cm $^{-3}$ and $T = 10^{-2}$ K. We refer to this region as a "buffer". We introduce this region to avoid possible spurious effects from an upper boundary condition (more details in the next section). The *left panel* in Figure 1 presents the $\rho - z$ plot for two different temperatures ($T = 1800$ K and 3000 K). The annotations near the right vertical axis (i.e. Buffer, Extension of Atm. and Atm.) refer to the case of $T = 3000$ K. The arrow outside the right vertical axis, annotated with "Right panel" in magenta, roughly shows the spatial scale of the schematic diagram of the atmosphere in

our computation box shown in the *right panel*. The *right panel* of Figure 1 will be explained in detail in §2.3.

To ensure robustness of our results given the numerical accuracy, we run simulations for a given initial condition with two resolutions. In the lower resolution simulations, the number of cells $N_{\text{cell}} = (N_x, N_y, N_z) = (256, 256, 512)$, while in the higher resolution simulations, $(N_x, N_y, N_z) = (512, 512, 1024)$. We choose the spatial scale of each single cell to be $\sim 0.1 H$ (where H is the scale height) for the lower simulation case and $\sim 0.05 H$ for the higher resolution. By filling the domain in this way, the total box size varies depending on what temperature we assume for the atmosphere. As will be explained in §2.1, we consider two different temperatures and the total box sizes of our models are given in Table 1.

Since our results are found to converge between the sim-

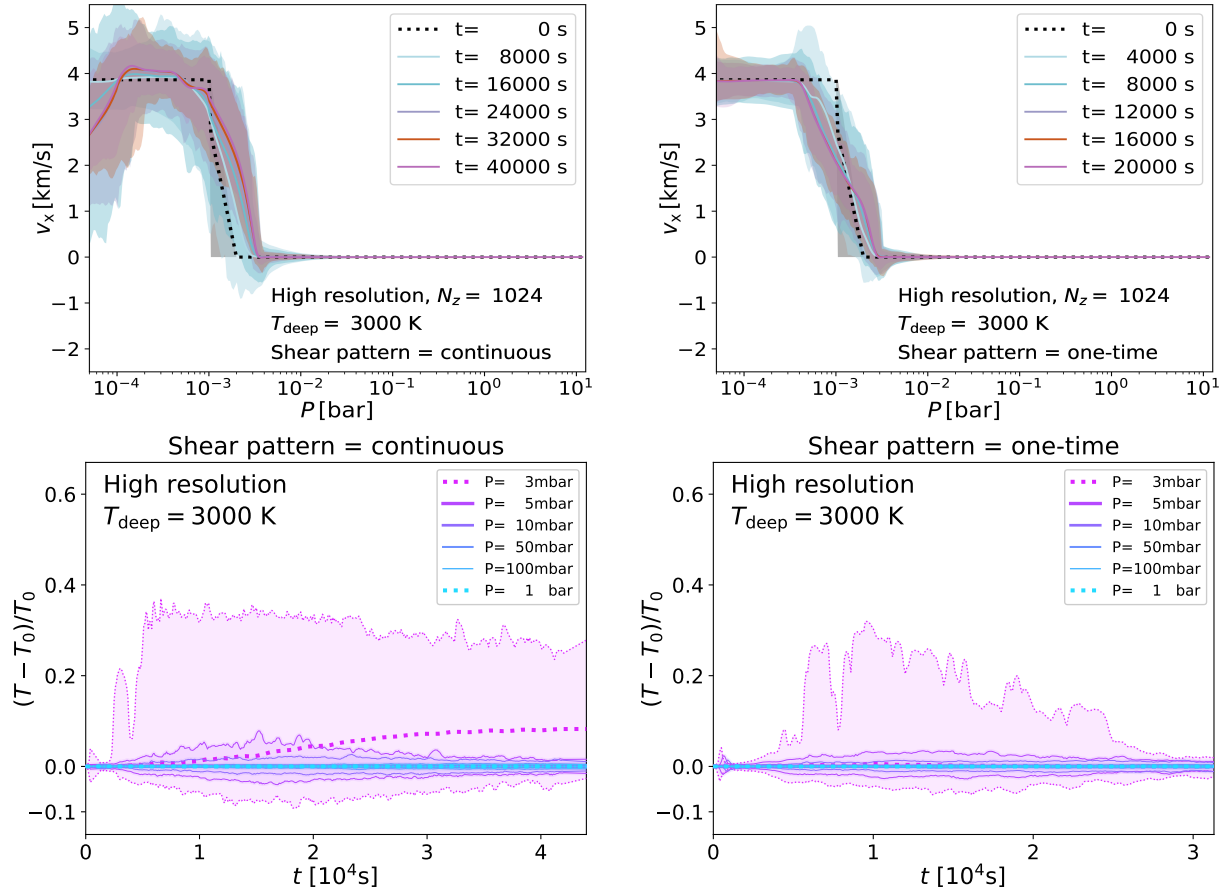


Figure 2. The velocities in the x direction (*top panels*) and the temperature (*bottom panels*) of the atmospheres with $T_{\text{deep}} = 3000$ K and $N_z = 1024$ with (“continuous”, *left panel*) and without (“one-time”, *right panel*) a momentum source. In the *left panel*, v_x at $0.1 \text{ mbar} \lesssim P \lesssim 1 \text{ mbar}$ is gradually driven to be c_s . The shaded regions around the horizontal average values (solid lines) demarcate the ranges between the maximum and minimum values at a given pressure and time. Note the different timescales on the x -axes between the two panels. The simulation with the “one-time” pattern stops at a shorter t since the atmosphere becomes steady earlier.

ulations with the two resolutions, in the result section we only focus on the atmosphere below $P \approx 1 \text{ mbar}$ (corresponding to $z \approx 10 H$) for further analysis in the high resolution simulations. We also discuss the differences between the simulations with the two resolutions in §4.1.

2.2 Boundary conditions

We consider a different boundary condition (BC) for each boundary. We use periodic BCs for the side boundaries. For the BC at the bottom, we employ a “hydrostatic” BC to provide the pressure support for the atmosphere against gravity. Here, the ghost cells outside the domain are initialized to satisfy hydrostatic equilibrium with adjacent cells, together with the equation of state. This is solved using the Newton-Raphson method with a tolerance of 10^{-12} . Furthermore we use a reflective BC on the velocity (or the momentum). These hydrostatic boundary conditions are described in Zingale et al. (2002).

For the top BC, we employ an inflow boundary condition in which ghost cells are updated to be the same as the uppermost inner cells, except for momentum. We only allow for incoming flows (i.e. gas with a negative vertical velocity v_z). However, if the gas at the boundary has a positive

vertical velocity $+v_z$, it is reset to be zero. In either case, the x and y components of velocities (v_x and v_y) are always zero at the boundary. The top BC is not relatively well-defined compared to the BCs at the other sides. Hence we introduce a buffer region on top of the atmosphere to place the atmosphere of our interest sufficiently far away from the upper boundary of the domain. This may increase the computational cost as the volume of the entire domain (low P atmosphere+buffer region) grows. However, this, along with the sponging applied in the buffer layer (see §2.3), ensures that the actual top BC does not matter and our results are robust against different choices for the upper BCs.

Employing these BCs, we have confirmed that our atmospheres stay in hydrostatic equilibrium (with no forced turbulence) sufficiently longer ($t > 1.5 \times 10^5$ s for low resolution simulations and $t > 3.0 \times 10^5$ s for high resolution simulations), than the total physical times considered in this paper, namely, $t < 5 \times 10^4$ s, which corresponds to a time long enough that our model atmospheres with the largest velocity gradient have become stable. Stability occurs at $t \lesssim 25 \tau_{\text{cross}}$ (see Equation 9 for the definition of τ_{cross}).

2.3 Shear prescription

It is found in numerical studies (e.g. Guillot & Showman 2002; Showman & Guillot 2002) that shear motions in the atmospheres of hot Jupiters can be caused by forcing due to the day-night temperature contrast. Furthermore, a typical Mach number at a level of $P = 1$ mbar is found to be around $\mathcal{M} \approx 1 - 2$ (e.g. Showman & Guillot 2002; Fromang et al. 2016). Motivated by these studies, we give an initial shear velocity in our model atmospheres as follows.

We consider a bulk shear motion only in the x direction. At $t = 0$ s, we give a constant shear velocity at a sound speed c_s at $P_{\text{sh}} = P \lesssim 1$ mbar. Below this region (higher P), we place a shear layer with a positive velocity gradient, i.e. $v_x(z = z_{i+1}) - v_x(z = z_i) > 0$ (cell index i , increasing with z). We refer to this region as “shear layer” throughout the paper. The velocity at the top of the shear layer is set to be c_s at $P = 1$ mbar, decreasing linearly down to $v_x = 0$ at the bottom of the shear layer. In other words, for two adjacent cells, $\Delta v_x / \Delta z = c_s / z_{\text{sh}} = \text{constant}$. Here, z_{sh} is the height of the shear layer. Furthermore, we consider a small number of zero velocity corrugations in the x and y directions (similarly to corrugations usually seen in billow clouds). This is to invoke more non-regular turbulent motions in every direction, albeit the corrugated pattern is regular. Velocity profiles (width, size and frequency of corrugation) inside the shear layer are unknown; future work specific to this will be necessary for more realistic modelling inside the shear layer. A schematic diagram illustrating the shear is shown in Figure 1. We emphasize that this forcing within the shear layer is only given at $t = 0$. Below the shear layer, starting typically from $P_{\text{sh,bottom}} \approx 2 - 3$ mbar ($P_{\text{sh,bottom}}$ refers to the pressure of the bottom of the shear layer), the atmosphere is assumed to be in static equilibrium with no initial velocity forcing.

At $t > 0$ s, we consider a momentum source in the x direction within $0.1 \text{ mbar} < P_{\text{src}} < 1 \text{ mbar}$ to continuously drive shear motions. This is to mimic the east-west stream found in many global circulation models, which is likely to last as long as the rotation of a planet is synchronized with the orbital motion. For the atmosphere within this pressure range, we add a certain amount of momentum to each cell equally at every time step such that horizontal average velocities in the $+x$ direction \bar{v}_x gradually approach $v_x = c_s$ over a certain time ($t_{\text{src}} = 1000$ s). While the atmosphere is dynamically evolving, it is possible that a mean motion of gas at any given time at some pressure happens to be supersonic in the $+x$ direction (i.e. $\bar{v}_x > c_s \hat{x}$, where \hat{x} refers to the basis vector in the x direction). Whenever that is the case, we do not apply this forcing to the gas at that pressure. This way, a bulk motion is gradually driven while small structures remain intact. We note that the lower pressure limit ($P = 0.1$ mbar) for the momentum input is arbitrarily chosen, but the atmosphere at $P > 1$ mbar is not sensitive to different choices of the lower limit. We can summarize this continuous forcing within $0.1 \text{ mbar} < P_{\text{src}} < 1 \text{ mbar}$ as follows. For gas at a given pressure P and time t with a mean motion \bar{v}_x , an external momentum (i.e. $\mathbf{S}_{\text{src}} \Delta t$ in Equation 2) is added to the momentum of the gas at each cell

$$\mathbf{S}_{\text{src}} = \bar{\rho} \frac{\max(0, c_s - \bar{v}_x)}{t_{\text{src}}}, \quad (4)$$

where “max()” indicates the maximum of the two values in

the parenthesis. To conserve the total energy of the gas, we take into account its additional energy accordingly (see Equation 3).

As an example, Figure 2 shows different evolutions of gas motions in the x direction and the temperature of the atmosphere with (“continuous”, left panel) and without (“one-time”, right panel) the additional momentum source. In the upper panel, we show v_x throughout the atmosphere at different times and in the lower panel the relative temperature variations with respect to the initial temperature T_0 at different pressure levels. In all the plots, the shaded regions around the horizontal average values (solid lines) demarcate the ranges between the maximum and minimum values at a given pressure and time. The size of the shaded regions is relevant for our study, along with the average values. This is because it can serve as a good indicator for how chaotic the atmosphere is due to turbulence. We can see some clear differences in both the v_x and the T plots. Among those, the most noticeable difference is in the larger shaded regions with the extra momentum source. This means that the momentum source clearly contributes to amplifying the effects and lifetime of turbulent motions, as we expect. From now on, we will only consider the “continuous” shear case.

For $P < 0.01$ mbar, we damp the velocity of the gas to $\mathbf{v} = 0$ in all directions. We use a damping scheme (or “sponge” damping) employed in the low Mach number code MAESTRO (Nonaka et al. 2010) and used in other studies (e.g. Zingale et al. 2009, 2011; Nonaka et al. 2012). This scheme was originally introduced to avoid a large growth in velocities in the low density regions of a stellar surface due to intense heating. See Section 4.3.1 in Almgren et al. (2008) for the equations used for the damping scheme. In our case, an unphysical surge in velocities can occur in the buffer region. This scheme serves to damp the large velocity wakes which would otherwise propagate towards the atmosphere and significantly affect its stability.

To sum up, the atmosphere is modelled such that:

At $t = 0$ (from $z = 0$ to larger z),

(i) $P_{\text{sh,bottom}} \lesssim P$: hydrostatic equilibrium with $\mathbf{v} = 0$ ($P_{\text{sh,bottom}}$ is determined by the size of the shear layer; see §2.4 below),

(ii) $1 \text{ mbar} \lesssim P \lesssim P_{\text{sh,bottom}}$: positive velocity gradient in the vertical direction,

(iii) $P \lesssim 1 \text{ mbar}$: $v_x = c_s$ and $v_y = v_z = 0$.

At $t > 0$, the atmospheric region at $P \lesssim 1$ mbar is affected by:

(i) $0.1 \text{ mbar} \lesssim P \lesssim 1 \text{ mbar}$: momentum source ($v_x \rightarrow c_s$);

(ii) $P \lesssim 0.01 \text{ mbar}$: sponge damping ($\mathbf{v} \rightarrow 0$).

2.4 Model parameters and initial condition

Our primary goal is to capture small-scale structures of turbulence and quantify the turbulent kinetic and heat energy flux which penetrates into the atmosphere. For this, we employ the analytic model in Youdin & Mitchell (2010) to determine the initial properties of our model atmospheres.

The atmospheres are characterized by two different temperatures, T_{deep} and T_1 . Note that we use the same notation as in Youdin & Mitchell (2010). T_{deep} is the temperature at the top of the atmosphere. Throughout this paper, we define

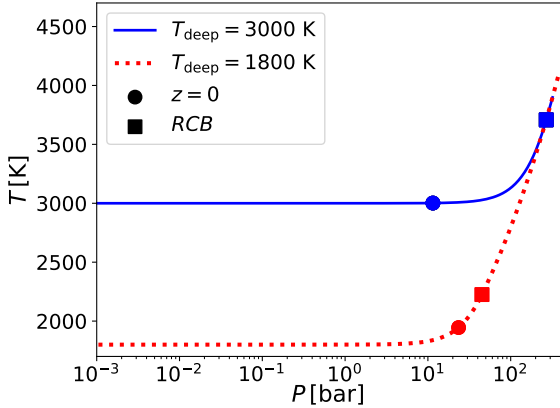


Figure 3. The initial $T - P$ profile for $T_{\text{deep}} = 3000$ K (blue solid lines) and $T_{\text{deep}} = 1800$ K (red dotted lines). We mark the pressure at $z = 0$ with circles, sharing the same line types and colors. The squares indicate the radiative-convective boundary (RCB), estimated using Equations 12 and 13 of Youdin & Mitchell (2010), for the given temperatures.

the top of the atmosphere to be at $P = 1$ mbar. On the other hand, T_1 is the temperature that convective regions would have at $P = 1$ bar, and it measures the internal entropy of the adiabat. Generally speaking, those two temperatures determine where the radiative-convective boundary (RCB) would be located. The pressure at the RCB P_{RCB} is lower for larger T_1 (higher entropy) or lower T_{deep} (strong irradiation).

In this study, our fiducial model assumes $T_{\text{deep}} = 3000$ K and $T_1 = 750$ K with $P \approx 12$ bar at $z = 0$. In addition, we explore a case with a lower temperature with $T_{\text{deep}} = 1800$ K for the same adiabat³. In Figure 3, we show the initial $T - P$ profiles of our models for $T_{\text{deep}} = 3000$ K (blue solid lines) and $T_{\text{deep}} = 1800$ K (red dotted lines), respectively. The circular marks represent the pressure at the bottom of our domain and the squares the radiative-convective boundaries (RCB) for the given temperatures.

We assume the atmosphere is made up of an ideal diatomic gas, with a mean molecular weight $\mu = 2.34$, following the equation of state,

$$P = \rho RT = (\gamma - 1)\rho e, \quad (5)$$

where $\gamma = 7/5$ and the gas constant $R = 3.6 \times 10^7$ erg g⁻¹ cm⁻¹. Again, e is the internal energy of the gas.

One important parameter left to decide is the height of the shear layer z_{sh} (see Figure 1) or $P_{\text{sh,bottom}}$, which determines the initial vertical gradient. In our simulations, eddy motions due to a Kelvin-Helmholtz instability are triggered by the non-zero velocity gradient in the shear layer ($v_x = c_s$ at $P \approx 1$ mbar and $v_x = 0$ at $P \approx P_{\text{sh,bottom}}$). For an incompressible flow, this is possible when the Richardson number is smaller than $1/4$ (Chandrasekhar 1961). The Richardson number Ri is defined as follows,

$$Ri = \frac{N^2}{(dv/dz)^2}, \quad (6)$$

³ For those two cases, $P_{\text{RCB}} = 268$ bar and $T_{\text{RCB}} = 3707$ K for $T_{\text{deep}} = 3000$ K and $P_{\text{RCB}} = 44$ bar and $T_{\text{RCB}} = 2224$ K for $T_{\text{deep}} = 1800$ K.

where N_{BV} represents the Brunt-Väisälä frequency,

$$N_{\text{BV}}^2 = \frac{\rho g^2}{P} [\nabla_{\text{ad}} - \nabla]. \quad (7)$$

In the above, ∇ refers to the lapse rate of the atmosphere, defined as,

$$\nabla = \left(\frac{d \ln T}{d \ln P} \right) \quad (8)$$

and the adiabatic lapse rate $\nabla_{\text{ad}} = 2/7$. From this expression, we can expect that if the vertical velocity gradient is chosen to be smaller, we start with a more unstable atmosphere. We choose the height of the shear layer to be small enough to give $Ri \lesssim 0.25$. In particular, we assume $Ri \approx 0.02, 0.1$ and 0.25 . These correspond to $N_{\text{sh,z}} = 6, 14$ and 24 within the layer for the higher resolution (hence half the cell number for the lower resolution case).

Each of our models is integrated until the atmosphere reaches a steady state. We assume the atmosphere becomes steady when variables including T and \mathbf{v} below $P \approx 3$ mbar do not change significantly. Typically, the atmospheres reach a steady state at $t \geq 10^4$ s for $Ri = 0.02$, the time being shorter with larger Ri . Note that this is still sufficiently shorter than the time for our model atmosphere to remain in equilibrium when there is no initial shear motion.

The model parameters and their initial values are summarized in Table 1.

3 RESULTS

In this section, we analyze the evolution of the thermodynamic properties of our model atmospheres. In particular, we focus on how much and how deep heat and kinetic energy fluxes can penetrate into the atmospheres. Additionally, we discuss shock formation in the atmospheres.

3.1 Development of Eddies

In all of our models, turbulent motions are created first inside the shear layer. The unstable motions spread downwards over time, but they are limited within $z \sim (1 - 2) H$, as shown in Figure 4. Each panel shows a 2-dimensional snapshot of a $x - z$ plane in the middle of our 3-dimensional box, for $Ri = 0.02$ (top panel), $Ri = 0.1$ (middle panel) and $Ri = 0.25$ (bottom panel) at $t/\tau_{\text{cross}} \approx 0.6, 2, 7, 12$ and 25 (from left to right). Here we use the crossing time of a sound wave across a pressure scale height as a characteristic time scale τ_{cross} , which we define as follows,

$$\tau_{\text{cross}} \approx 2\pi \frac{H}{c_s} = \begin{cases} 1734 \text{ s}, & T_{\text{deep}} = 3000 \text{ K}, \\ 1343 \text{ s}, & T_{\text{deep}} = 1800 \text{ K}. \end{cases} \quad (9)$$

The top corresponds to a level of $P \approx 0.3$ mbar and the initial shear layer extends below from $P \approx 1$ mbar. The plots are color-coded according to the temperature from blue (lower T) to red (higher T). The vertical line with T-shaped heads in each panel indicates the $2H$ spatial scale. The temperatures in the atmospheres with lower Ri are generally higher at a given time. Furthermore, eddies at larger scales break up into smaller eddies. These are typically expected

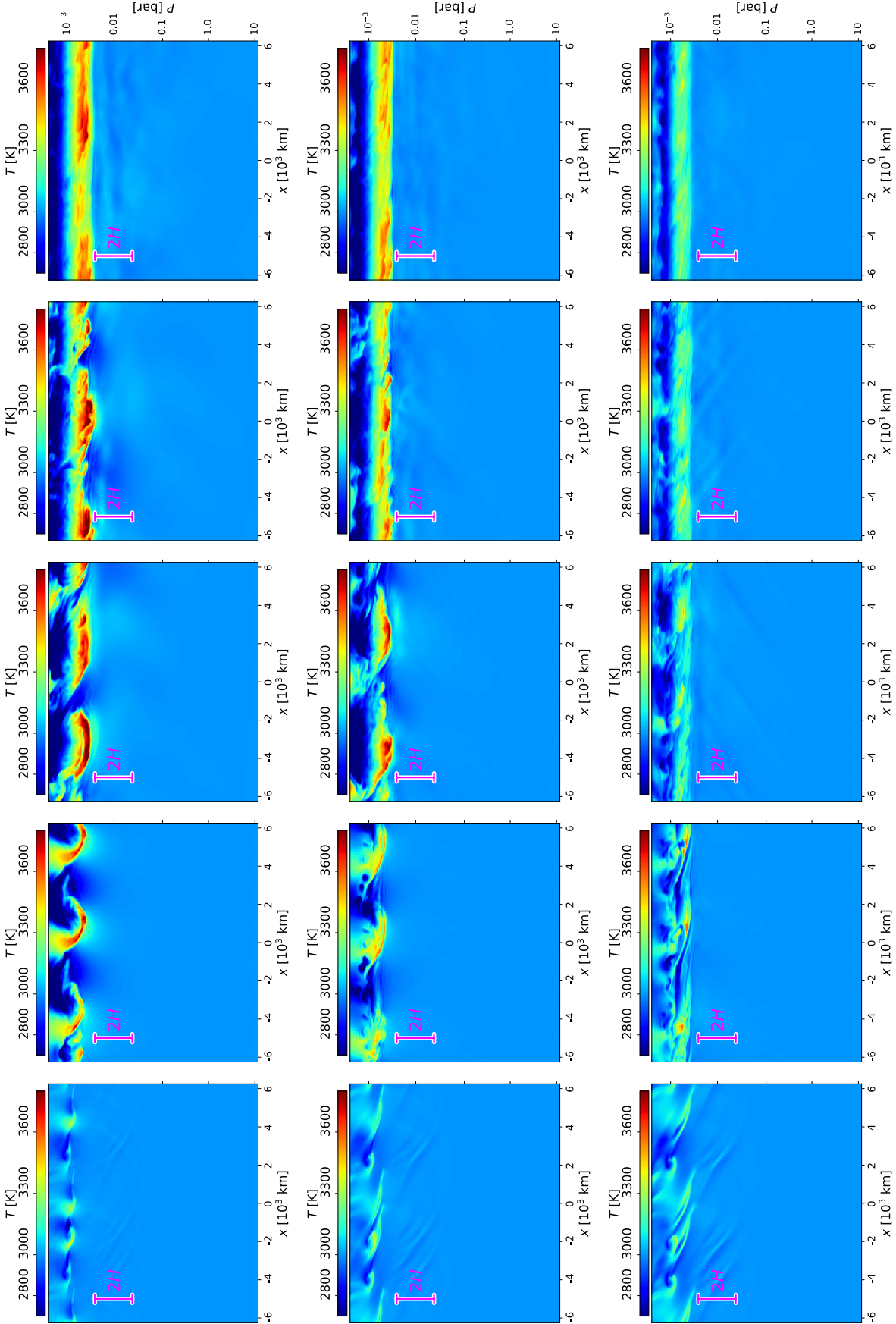


Figure 4. 2-dimensional snapshots for $x - z$ plane in the middle of our 3-dimensional domain for $Ri = 0.02$ (top panel), $Ri = 0.1$ (middle panel) and $Ri = 0.25$ (bottom panel), at $t/\tau_{\text{cross}} \approx 0.6, 2, 7, 12$ and 25 (from left to right). τ_{cross} is a characteristic time scale for eddy motions, which is defined in Equation 9. The top of each panel corresponds to a level of $P \approx 0.3$ mbar and the initial shear layer extends below from $P \approx 1$ mbar. The color coding indicates the temperature from lower (blue) to higher (red) T . The vertical line with T-shaped head in each panel represents the 2H spatial scale.

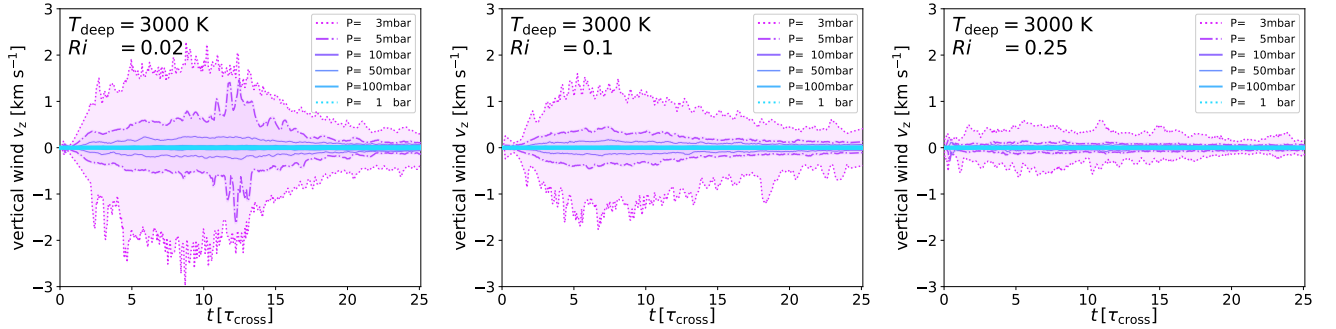


Figure 5. The average vertical velocity \bar{v}_z at different pressures for (from left to right) $Ri = 0.02$, 0.1 and 0.25 . The boundaries of the shaded regions show the maximum and the minimum values around the average values (solid lines) at a given time and pressure.

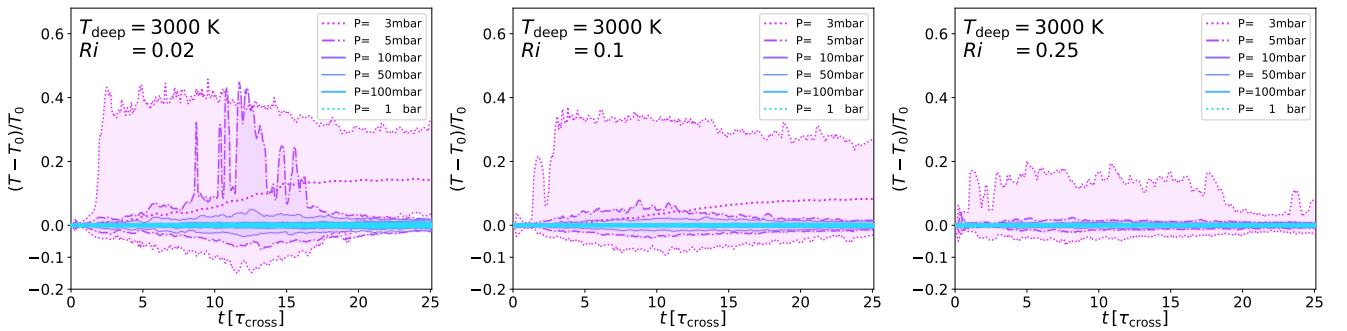


Figure 6. Fractional changes of T relative to the temperature at $t = 0$ (denoted by T_0) for the same pressures as in Figure 5. The shaded regions have the same meaning as before.

in a standard picture of turbulence. It is noticeable that distinctive variations in T are limited within a vertical range of $1 - 2 H$, i.e., $P \lesssim 10$ mbar. In our models, $P \approx 2.5$ mbar at $z = z_{1 \text{ mbar}} - H$, where $z_{1 \text{ mbar}}$ is the height at $P = 1$ mbar, and $P \approx 6$ mbar at $z = z_{1 \text{ mbar}} - 2H$. In our model we do not consider convective bulk motions in the vertical direction. That means that heat energy transfer can only occur via turbulent motions of the gas. In light of this, we can see from the slice plots that the atmosphere below $P \approx 10$ mbar is not significantly affected by turbulent motions driven in the shear layer near its top. Note that the temperature evolution shown in the plot is not only directly indicative of heat fluxes, but it also gives us a sense of the overall effect of turbulence. This will be shown more clearly in the following sections.

3.2 Velocity and temperature variation

It has been suggested that turbulent mixing due to the non-linear Kelvin–Helmholtz instability plays an important role in the penetration and dissipation of kinetic energy. Vertical motions of gas are a primary factor to determine in which direction the kinetic and heat energy fluxes (along with temperature variations) propagate. Therefore, it is important to understand first how vertical velocities in our atmospheres evolve and how temperatures vary over time under the presence of the shear motion.

Figure 5 shows the average vertical velocity \bar{v}_z at different pressures for (from left to right) $Ri = 0.02$, 0.1 and 0.25 . Positive (negative) values indicate upward (downward)

movements. Note that $P \approx 3$ mbar corresponds to the bottom of the shear layer for $Ri = 0.25$, whereas for lower Ri the shear layers are positioned at $P \lesssim 3$ mbar. The shaded regions are bounded by the maximum and the minimum values around the average values (solid lines) at a given time and pressure. Shaded regions in other plots of this type below will have the same meaning. A general trend is that the magnitude of fluctuations in v_z ($|v'_z| = |\bar{v}_z - v_z|$) increases up to $t/\tau_{\text{cross}} \approx 5 - 10$, but gradually decreases afterwards. The velocity fields symmetrically fluctuate and $|v'_z|$ decreases by a factor of 3–5 from one pressure to the next higher pressure chosen in the plots. Meanwhile, average vertical motions remain almost zero at those pressure levels. This means that there is no dominant bulk motion in the vertical direction and eddies are confined within a small volume (a few mbar vertically). This is also shown in Figure 4. At $t/\tau_{\text{cross}} \gtrsim 10$, $|v'_z|$ does not increase, but rather decays or stays constant.

We next present the relative changes of T with respect to the temperature at $t = 0$ (denoted by T_0) in Figure 6 for the same pressures as in Figure 5. Somewhat contrary to the symmetric changes in \bar{v}_z , as Ri decreases (left and middle panel), turbulence leads to a more positive temperature fluctuation T' at $P \approx 3$ mbar (corresponding to the bottom of, or slightly below, the shear layer). However this is not clearly seen for the models with $Ri = 0.25$ (right panel) and at $P \gtrsim 5$ mbar for $Ri = 0.02$ and 0.1 .

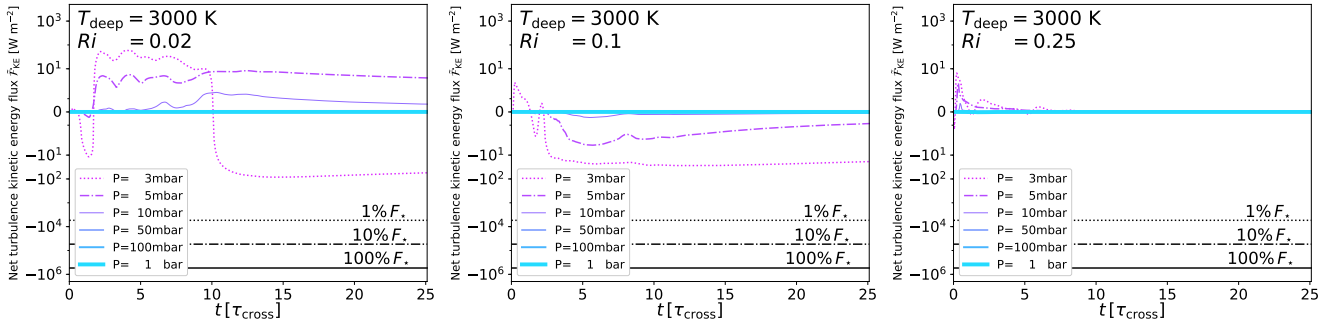


Figure 7. Time evolution of the turbulence kinetic energy flux \tilde{F}_{KE} for $Ri = 0.02$ (left panel), $Ri = 0.1$ (middle panel) and $Ri = 0.25$ (right panel). The horizontal lines near bottom indicate 1% ($\approx -10^6 \text{ W m}^{-2}$, solid horizontal line), 10% ($\approx -10^5 \text{ W m}^{-2}$, dot-dashed line) and 100% ($\approx -10^4 \text{ W m}^{-2}$, dotted line) of an incoming stellar flux at $T = 3000 \text{ K}$.

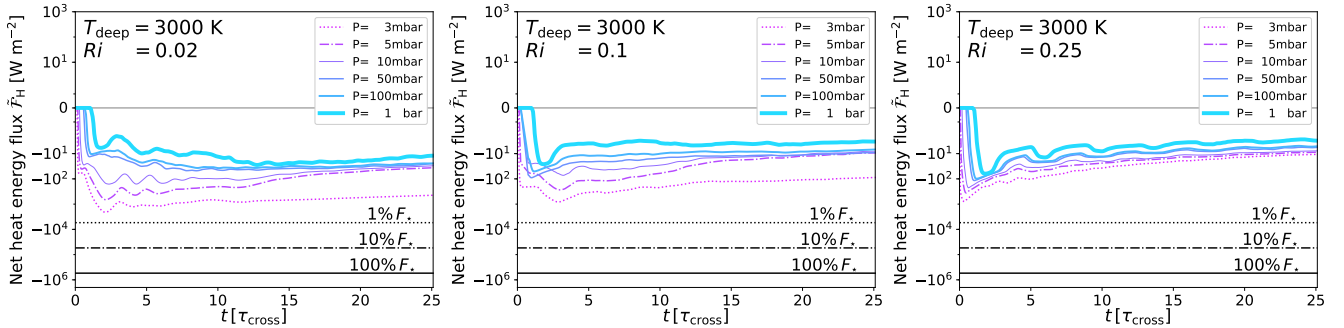


Figure 8. Time evolution of the turbulence heat flux \tilde{F}_H calculated using Equation 11 for $Ri = 0.02$ (left panel), $Ri = 0.1$ (middle panel) and $Ri = 0.25$ (right panel).

3.3 Kinetic energy and heat flux transport due to turbulence

Figures 7 and 8 show the time-averaged turbulence vertical kinetic energy flux \tilde{F}_{KE} and the turbulence vertical heat flux \tilde{F}_H , respectively. In the flux figures, the three horizontal lines near the bottom indicate 1% ($\approx -10^6 \text{ W m}^{-2}$, solid horizontal line), 10% ($\approx -10^5 \text{ W m}^{-2}$, dot-dashed line) and 100% ($\approx -10^4 \text{ W m}^{-2}$, dotted line) of the incoming stellar flux F_{\star} at $T = 3000 \text{ K}$. We first define an instantaneous kinetic energy flux \tilde{F}_{KE} (Hannoun et al. 1988), while \tilde{F}_H defines the heat flux as $\rho c_p v_z T'$ at t and P as follows,

$$\tilde{F}_{KE}(t, P) = \overline{\rho \tilde{E}_{KE} v'_z}, \quad (10)$$

$$\tilde{F}_H(t, P) = \overline{\rho c_p v_z T'}, \quad (11)$$

where c_p is the specific heat capacity at constant pressure, $c_p = R/\nabla_{ad}$. \tilde{E}_{KE} is the turbulence specific kinetic energy,

$$\tilde{E}_{KE} = \frac{1}{2}(v_x'^2 + v_y'^2 + v_z'^2). \quad (12)$$

Using then the instantaneous fluxes extracted from the output data at specific time intervals ($\Delta t/\tau_{cross} \approx 0.06$)⁵, we

calculate a time average of the fluxes at a given t and P as,

$$\tilde{F}(t, P) = \frac{1}{t} \sum_{t'=0}^{t'=t} \tilde{F}(t', P) \Delta t. \quad (13)$$

The turbulent kinetic energy flux \tilde{F}_{KE} in Figure 7 at $Ri = 0.25$ (right panel) is nearly zero throughout the atmosphere below the shear layer. On the other hand, for the lower Ri (left and middle panels), the magnitudes of the fluxes $|\tilde{F}_{KE}|$ are smaller at higher P ⁶. The fluxes at $P \approx 3 \text{ mbar}$ for both Ri 's are the largest and remain constant, but they are at most 0.01–0.001% of F_{\star} . This means that the continuous shear forcing at the top keeps exciting eddy motions, but confined at $P \lesssim 10 \text{ mbar}$, then the turbulence kinetic energy rapidly dissipates into heat. Next, we quantify the turbulence heat energy flux \tilde{F}_H .

Unlike the kinetic energy flux, the turbulence heat flux \tilde{F}_H in Figure 8 propagates downwards at all pressures with its magnitude smaller for higher Ri . However, this flux is not significant, roughly $\lesssim 0.01\%$ of the incoming flux. Furthermore, \tilde{F}_H for $Ri = 0.25$ at all pressures gradually converges to zero. Only for $Ri = 0.01$, \tilde{F}_H at $P \approx 3 \text{ mbar}$ maintains a 0.1% level. The fact that \tilde{F}_H remains constant at later times

etc.) and some derived variables (e.g., entropy and etc.). We post-process the data for more model-specific variables, such as \tilde{F} .

⁶ We find that \tilde{F}_{KE} in some deeper regions ($5 \leq P \leq 10 \text{ mbar}$) becomes positive. We believe that this is mostly due to small random fluctuation of \tilde{F}_{KE} around zero.

⁴ Hurlburt et al. 1984 defines the heat flux such that positive \tilde{F}_H is directed downward. Notice the negative sign in their definition.

⁵ To maximize the code speed, the current default set-up of the code allows to print out the main state variables (e.g. ρ , T and

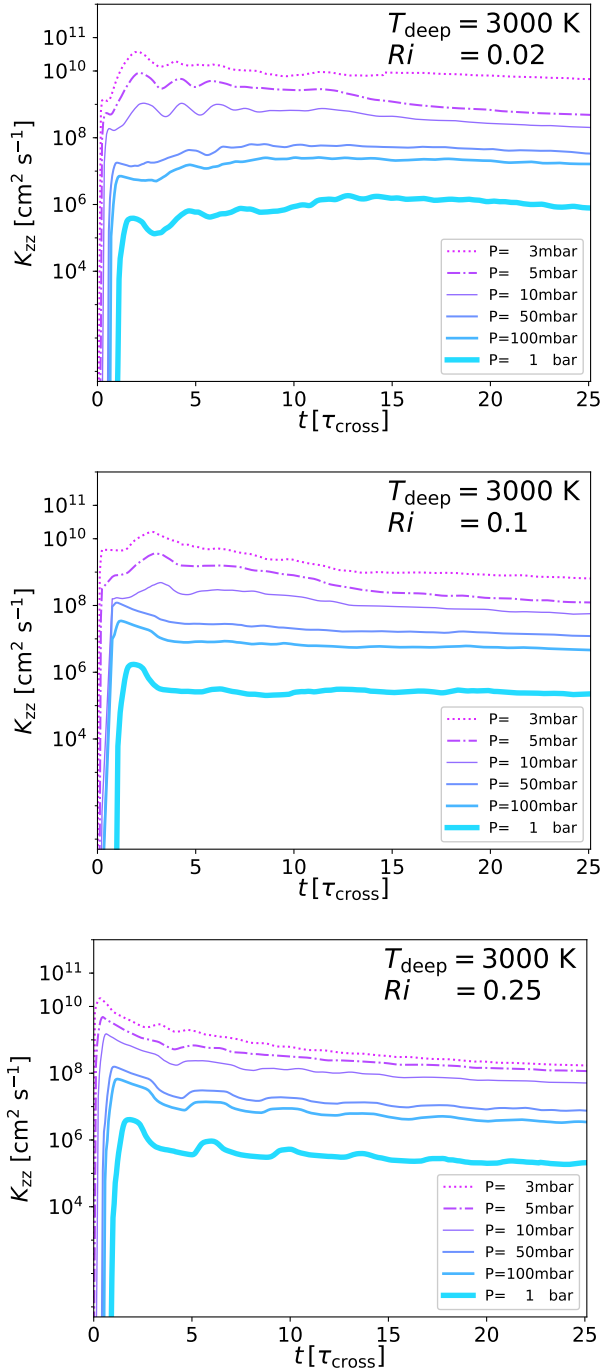


Figure 9. The time evolution of the eddy diffusion coefficient K_{zz} for $Ri = 0.02$ (top panel), $Ri = 0.1$ (middle panel) and $Ri = 0.25$ (bottom panel).

means an unvarying inflow rate of the instantaneous flux \tilde{F}_H over the unit time (consider Equation 13 with constant \tilde{F}_H).

Overall, our results suggest that turbulence due to the shear motion near the top cannot lead to deep penetration of the energy flux, which remains confined in a vertical spatial scale of $\sim 2H$. The atmosphere below $P = 10$ mbar is barely affected by the turbulent motion at $P \approx 1 - 3$ mbar.

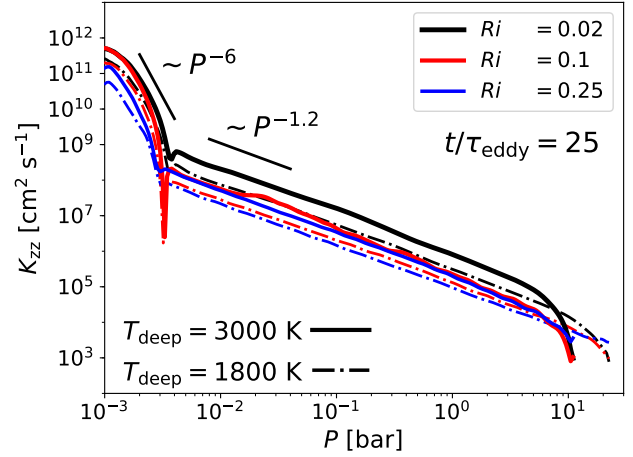


Figure 10. K_{zz} as a function of P for our atmosphere models with $T_{\text{deep}} = 3000$ K (solid lines) and $T_{\text{deep}} = 1800$ K (dot-dashed lines).

3.4 Eddy diffusion coefficient

Our numerical experiments have shown that heat energy transport via turbulence by a forced shear layer is not a large-scale effect, but is rather locally confined within a vertical range of $\sim 2H$. However, it is still worth quantifying the eddy diffusion coefficient K_{zz} for negative F_H in the atmosphere. We estimate K_{zz} by combining equation (20) in Youdin & Mitchell (2010),

$$F_H = -K_{zz}\rho T \frac{dS}{dz}, \quad (14)$$

with the time-averaged heat flux \tilde{F}_H (Equations 11 and 13). These two equations give the following expression for K_{zz} ,

$$K_{zz} = \left| \frac{\sum_{t'=0}^{t'=t} \overline{\rho c_p v_z T'} (\Delta t/t)}{\rho T \left(\frac{\Delta S}{\Delta z} \right)} \right|, \quad (15)$$

where $\frac{dS}{dz}$ is estimated as follows,

$$\frac{\Delta S}{\Delta z}(z = h) = \frac{S(z = h + \Delta z) - S(z = h - \Delta z)}{2\Delta z}. \quad (16)$$

Based on the time-averaged heat fluxes found in our models, we find (see Figure 9) that for $Ri = 0.01$ (upper panel), $K_{zz} \approx 10^8 - 10^{10} \text{ cm}^2 \text{ s}^{-1}$ at a few Pmbar pressures, decreasing down to $K_{zz} \approx 10^5 \text{ cm}^2 \text{ s}^{-1}$ at $P = 1$ bar. There is no significant difference between $Ri = 0.1$ (middle panel) and $Ri = 0.25$ (bottom panel), except for $P = 3$ mbar. These values are reasonably consistent with Spiegel et al. (2009), where they estimate a $K_{zz} \sim 10^7 - 10^{11} \text{ cm}^2 \text{ s}^{-1}$ to be necessary to maintain sufficient TiO in the upper atmospheres ($P \approx$ a few mbar) for thermal inversion.

These estimates, however, do not clearly inform us on how the coefficient K_{zz} varies with pressure. To find the dependence of K_{zz} on P , we show K_{zz} as a function of P for our atmospheric models with $T_{\text{deep}} = 3000$ K (solid lines) and $T_{\text{deep}} = 1800$ K (dot-dashed line) in Figure 10. We see that we have different P dependences at $P \gtrsim 3 - 4$ mbar and $P \lesssim 3 - 4$ mbar for all the models. K_{zz} at $P \lesssim 3 - 4$ mbar

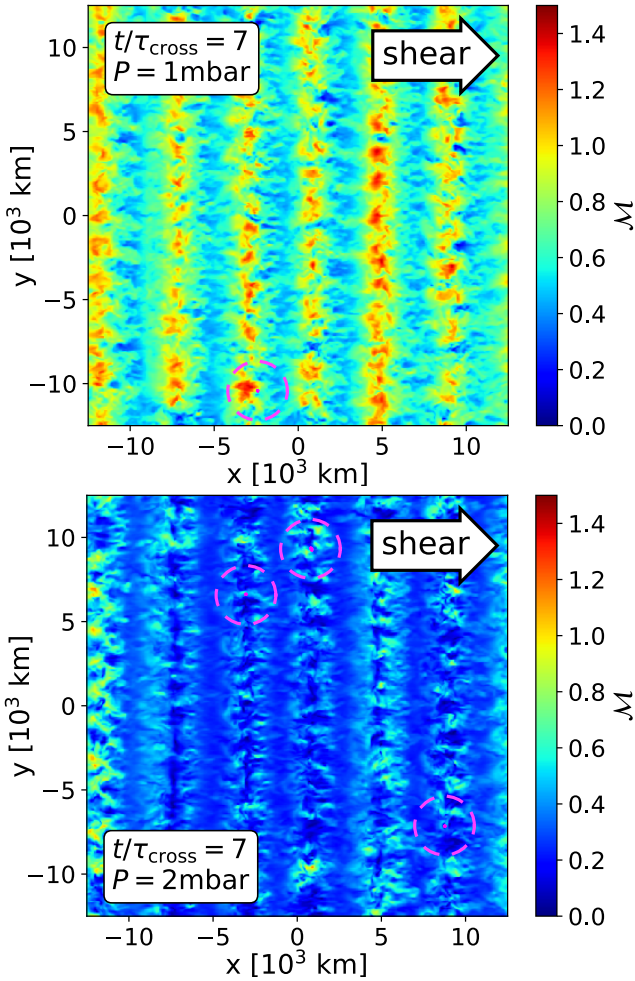


Figure 11. Horizontal slice plots for \mathcal{M} in the atmosphere with $T_{\text{deep}} = 3000$ K at $P = 1$ mbar (*top* panel) and $P = 2$ mbar (*bottom* panel) at $t = 7 \tau_{\text{cross}}$ when the initial $Ri = 0.02$. The arrow at the top-right corner indicates the direction of continuous shear motion. The magenta circles indicate where shocks are detected. The plots are color-coded based on the magnitude of \mathcal{M} .

dramatically declines, followed by a relatively mild decrease in the deeper atmosphere. Such steepness near the top is clearly due to chaotic eddy motions. Interestingly, K_{zz} for $Ri = 0.02$ (black lines) and $Ri = 0.25$ (blue lines) throughout the atmosphere have almost the same dependence on P , only differing by a factor of ~ 5 in magnitude. On the other hand, K_{zz} for $Ri = 0.1$ (red lines) shows a transitional behavior between that for $Ri = 0.02$ (black lines) and $Ri = 0.25$ (blue lines): the lines for $Ri = 0.1$ are very close to those for $Ri = 0.02$ at $P \lesssim 3 - 4$ mbar whereas they are still lingering near the lines for $Ri = 0.02$ at $P \gtrsim 3 - 4$ mbar. From this, we may be able to conjecture the following: 1) $Ri = 0.1$ could be a characteristic value below which the heat flux starts effectively penetrating into the deeper region and 2) inflow of a heat flux in the inner region may occur via episodic jumps, rather than by a gradual growth. However, it is important to emphasize that our conjectures are made only based on our models, which cover a subset of the whole parameter space. In order to find more general trends of K_{zz} (e.g. how K_{zz} would increase in atmospheres for $Ri < 0.01$,

in particular whether it would gradually increase or whether there would be another lingering phase like the one we find for $Ri = 0.25 - 0.02$), we need to explore a larger parameter space with different initial conditions, which we will leave for future work.

Assuming K_{zz} follows a power law of P such that $K_{zz} \propto P^{-\alpha}$, the following provides a fit for K_{zz} ,

$$K_{zz} \approx \begin{cases} 5 \times 10^8 \beta \left(\frac{P}{P_L}\right)^{-6} & \text{cm}^2 \text{ s}^{-1} & P < P_L, \\ 5 \times 10^8 \beta \left(\frac{P}{P_L}\right)^{-1.2} & \text{cm}^2 \text{ s}^{-1} & P \geq P_L, \end{cases} \quad (17)$$

where β is a normalization factor, possibly depending on T_{deep} and the velocity gradient due to shear (Ri). As mentioned above, at least for $Ri = 0.02$ and $Ri = 0.25$, β is a constant, differing by around 5. P_L can be approximately found to be $P_L \approx P$ at $z = z_1 \text{ mbar} - 1.5H$.

The convergence of K_{zz} at the bottom ($P \approx 10 - 30$ bar), along with the sharp decrease, in all our models is probably due to the boundary condition. This drop has been found in Youdin & Mitchell (2010) for negative α (see their Figure 7), but near quite large pressures at which $\nabla = \nabla_{\text{ad}}/2$. In our models, the pressure which satisfies the condition corresponds to $P \approx 270$ bar (45 bar) for $T_{\text{deep}} = 3000$ K (1800 K), which is much higher than P at the bottom.

3.5 Shock formation

Here we consider the formation of shocks in our atmosphere. We use a basic multi-dimensional shock detection algorithm (Colella & Woodward 1984; Colella 1990) embedded in the code CASTRO to trace shocks. Overall, we find that shocks form, but they are sporadic (in space) and transient (in time).

Shocks form within a range of $P \lesssim 2.5$ mbar and the fraction of the areas where shocks are detected, defined as the ratio of the number of cells identified with shocks to the total number of cells at a given pressure, remains below the $10^{-3} - 10^{-4}$ % level even in the most unstable atmosphere. We show horizontal slice plots for \mathcal{M} in the atmosphere with $T_{\text{deep}} = 3000$ K in Figure 11 at $P = 1$ mbar (*top* panel) and $P = 2$ mbar (*bottom* panel) at $t = 7 \tau_{\text{cross}}$. This figure is made for the model with $Ri = 0.02$, but the other models look very similar. The color indicates the magnitude of \mathcal{M} as given in the color bar. We also mark where shocks form using magenta dotted circles. They are local and scattered.

The shocks last longer in the atmosphere starting with smaller Ri , but they are no longer detected at $t \gtrsim 12 \tau_{\text{cross}}$ for $Ri = 0.02$. This is visualized in Figure 12. This figure shows the largest pressure at which shocks form (P_{max}) as a function of time in our models with $T_{\text{deep}} = 3000$ K (solid lines) and $T_{\text{deep}} = 1800$ K (dotted line). The times when the lines cross the $P = 1$ mbar level correspond to moments when there are no shocks in the atmospheres. As clearly shown in the figure, the shocks cannot penetrate deeper than $P \approx 2$ mbar and disappear rather quickly.

From the above, we conclude that shock formation is insignificant; therefore, shocks are not expected to affect the evolution of the atmospheres. Interestingly, even though Fromang et al. (2016) investigated shocks based on different atmosphere models and criteria for shock formation, both studies suggest similar conditions for shock formation.

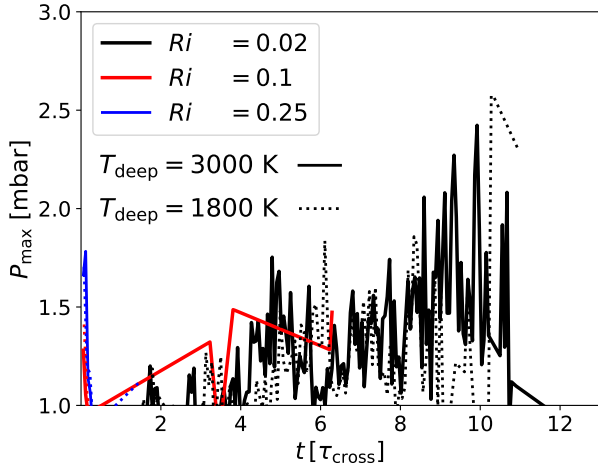


Figure 12. The maximum pressure at which shocks are detected (P_{\max}) as a function of time in our models with $T_{\text{deep}} = 3000$ K (solid lines) and $T_{\text{deep}} = 1800$ K (dotted line). The times at which the lines hit the bottom (i.e. at $P = 1$ mbar) correspond to times when there are no shocks in the atmosphere.

Shocks are not found in their low resolution simulations. However, at resolution high enough to resolve finer structures of jets, they find instabilities which cause velocity fluctuations, ultimately transforming into weak shocks at $P \approx$ a few mbar. This trend (i.e. resolution dependence and weak shocks confined to lower pressures) is in good agreement with the findings from our simulations.

4 DISCUSSION

4.1 Comparison: different resolutions and the role of T_{deep}

In this section, we compare our simulations between different resolutions and discuss the role of T_{deep} .

(i) Resolution

As mentioned in §2.4, to test the numerical reliability of our results, we performed every set of our simulations with two resolutions ($N_z = 1024$ and 512). We find converging results between the high and low-resolution simulations, which adds more robustness to our results. More specifically: in the low resolution simulations it is found that fluctuations in all the variables are generally larger at the initial times and inside the shear layer; however, when the atmosphere becomes steady, the final values of the variables are in a quite good agreement with the higher resolution simulations. One difference worth noting is the maximum depth at which shocks form, or P_{\max} . In the low resolution simulations, the depth extends to $P \approx 5$ mbar and the shocks last longer, roughly by a factor of 2 than the higher resolution runs, and more shocks are detected (the fraction of atmospheric area containing shocks goes up to $10^{-1}\%$). Hence the formation of shocks can be overestimated if the resolution is not sufficiently small.

(ii) T_{deep}

The evolution of all the relevant variables mentioned so

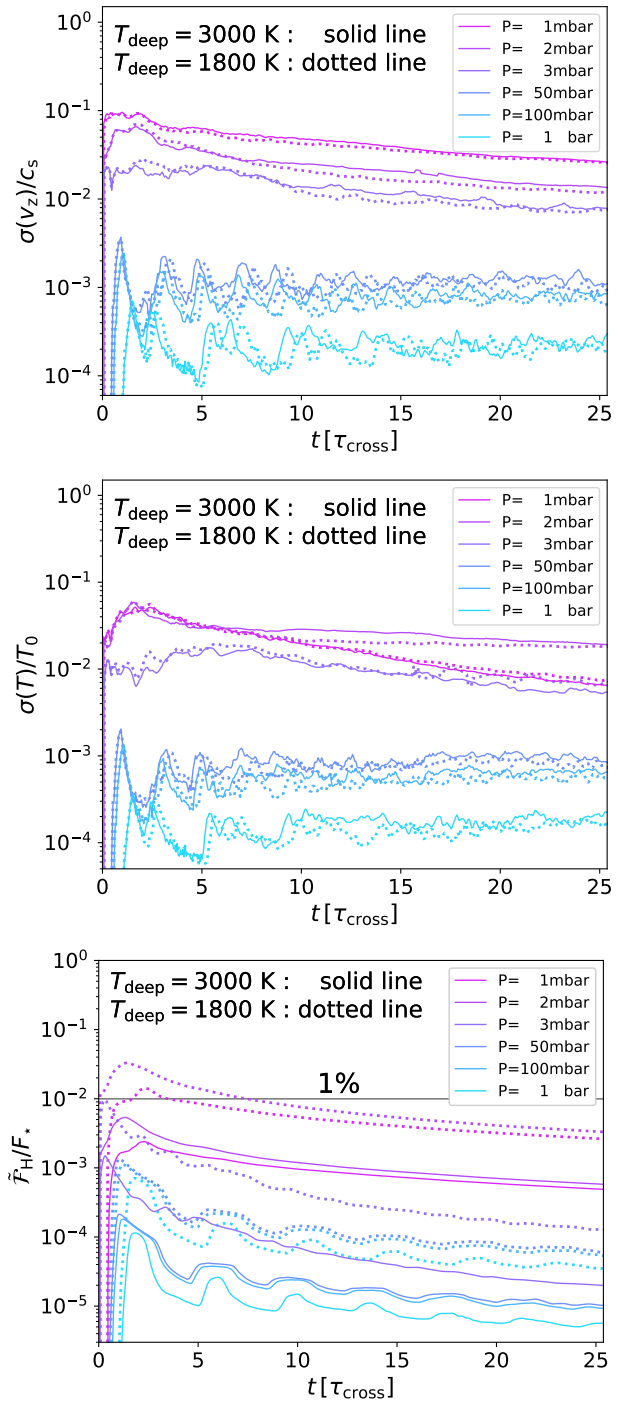


Figure 13. Root-mean-square (σ) of v_z and T , as well as the heat flux, normalized by c_s , T_0 , and F_\star as a function of time for the two models with different T_{deep} at different pressures. The black horizontal line in the *bottom* panel corresponds to 1% of F_\star .

far, namely T , v_z and the energy fluxes, are almost identical⁷. Among those variables, we show the RMS σ of v_z and T and the heat fluxes for the two models in Figure 13. For a

⁷ Note that Δl (with respect to H) for the models with different T_{deep} and their initial $T - P$ profiles (such as $P(z = 0)$) are not exactly the same. The number of cells per scale height for $N_z =$

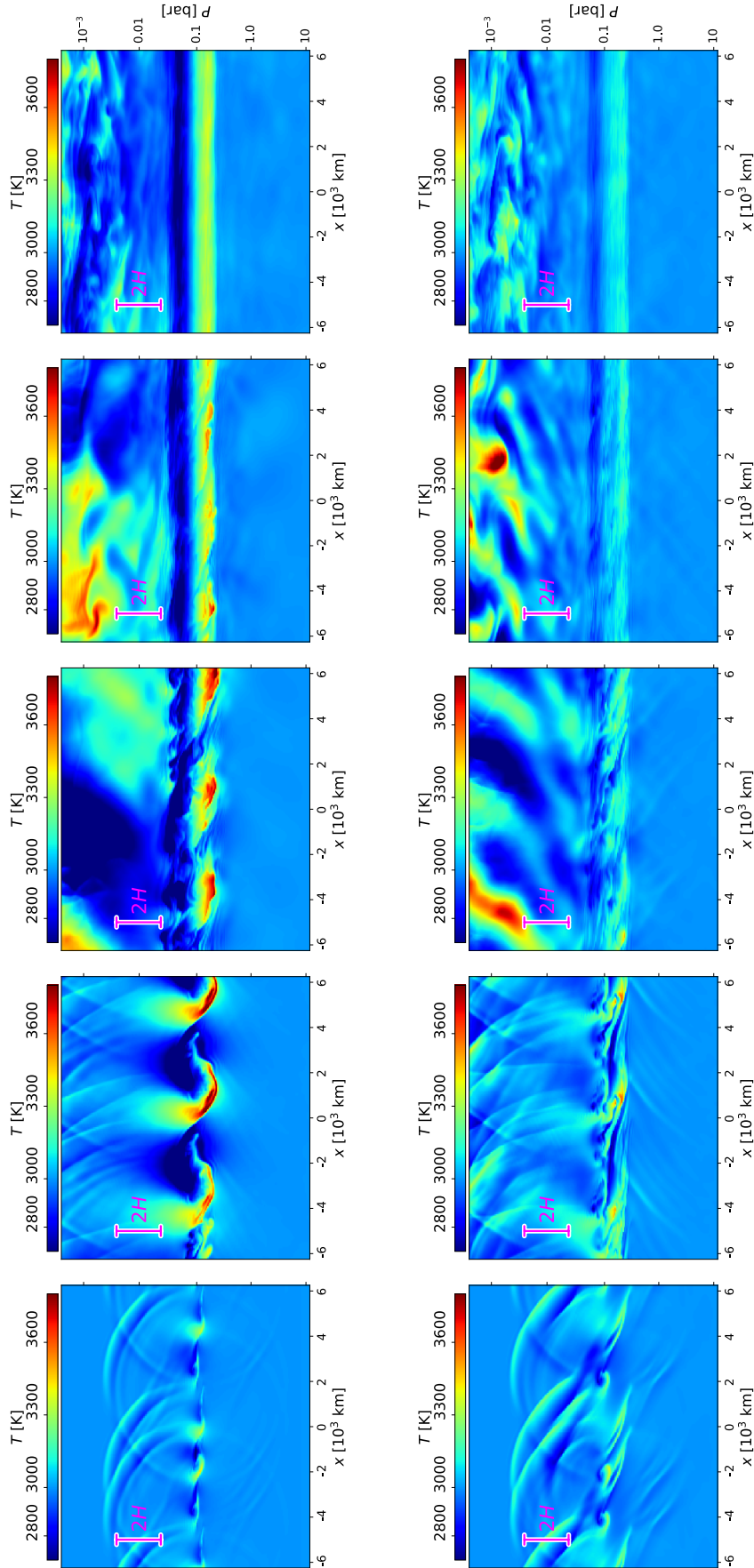


Figure 14. 2-dimensional slice plots showing the temperature for our two models, but with the shear layer at a deeper level, $P_{\text{sh}} = 100$ mbar, at the same times as in Figure 4, i.e., $t/\tau_{\text{cross}} = 0.6, 2, 7, 12$ and 25 (from left to right). The *upper* panel presents the model for $Ri = 0.02$ and the *lower* panel for $Ri = 0.25$, respectively.

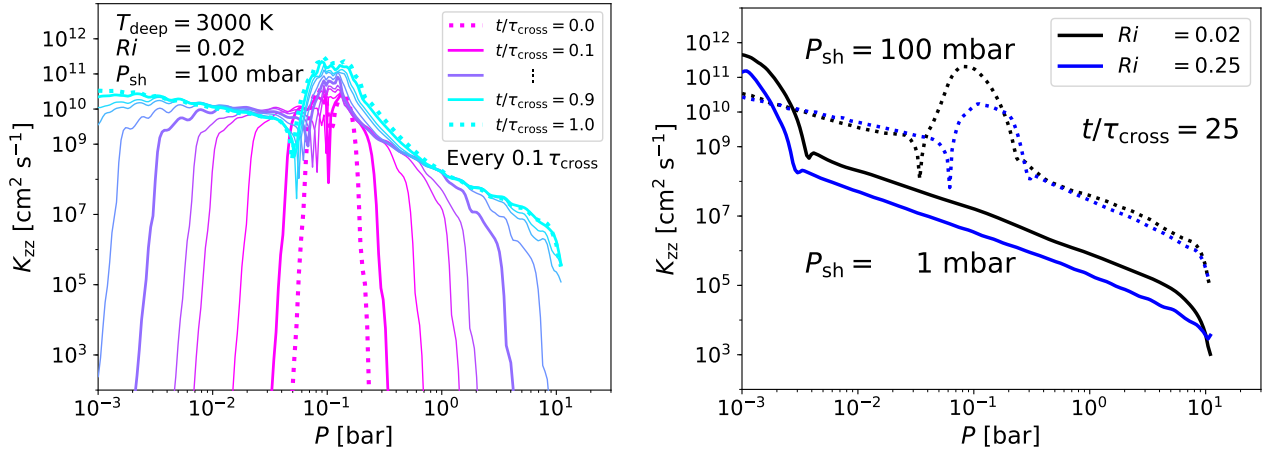


Figure 15. *Left panel:* time evolution of K_{zz} every $0.1 t/\tau_{\text{cross}}$ for $0 \leq t/\tau_{\text{cross}} \leq 1$ (the dotted lines indicate $t/\tau_{\text{cross}} = 0$ and 1 and the solid lines for the intermediate times). *Right panel:* K_{zz} as a function of P for the atmospheres with different P_{sh} for $Ri = 0.02$ (black lines) and $Ri = 0.25$ (blue lines). The dotted lines indicate the models with $P_{\text{sh}} = 100$ mbar and the solid lines those with $P_{\text{sh}} = 1$ mbar.

self-similar comparison, we normalize each value by a characteristic variable in the same dimension, such as T_0 , c_s and F_\star . The black horizontal line in the *bottom* panel indicates 1% of F_\star . T and v_z are found to be very comparable whereas $\tilde{\mathcal{F}}_{\text{H}}/F_\star$ shows some discrepancies. Indeed, it is because the magnitudes of $\tilde{\mathcal{F}}_{\text{H}}$, not $\tilde{\mathcal{F}}_{\text{H}}/F_\star$, for the two models are very similar. This may mean that, as long as the Mach number of the horizontal shear motion at top is the same, the amount of heat flux reaching a certain pressure level is independent of T_{deep} . This argument will need to be further explored in future work.

4.2 Turbulence in the deep regions

So far, we have focused on turbulence initially created at $P_{\text{sh}} \approx 1$ mbar. However, we cannot rule out the possibility that turbulence is generated more deeply. In stable stratified atmospheres, turbulence can be caused by a breakdown of internal buoyancy waves, like in the atmospheres of the Earth, Mars and Venus (Izakov 2001, 2002). In many global model simulations for hot Jupiters, it has been found that transonic zonal winds extend vertically down to $P \approx 1$ bar (e.g. Showman et al. 2009; Rauscher & Menou 2010, 2012; Fromang et al. 2016). For example, Showman et al. (2009) find from their global 3-dimensional numerical simulations peak zonal wind speeds of 3.5 km s^{-1} at $P \approx 10 - 100$ mbar (corresponding to $\mathcal{M} > 1$ assuming $T = 1200 \text{ K}$) and Fromang et al. (2016) find Ri at $P \approx 1$ bar can be as low as $0.1 - 0.25$. This means that atmospheres at those pressure levels may also be subject to shear instabilities. In addition, based on evolution calculations with the MESA code, Komacek & Youdin (2017) studied the impact of internal heating on the radius evolution of hot Jupiters by systematically varying the depth and intensity of internal heating. They find that heating at $P \gtrsim 10$ bar is required to keep hot Jupiters inflated as large as their observed radii. This

also supports the importance of turbulence at deeper atmospheric levels.

To explore the role of turbulence in the deeper regions, we additionally perform two simulations for the hotter atmosphere ($T_{\text{deep}} = 3000 \text{ K}$) with a shear layer at $P_{\text{sh}} \approx 100$ mbar, instead of $P_{\text{sh}} \approx 1$ mbar. In this experiment, we only consider $Ri = 0.25$ and $Ri = 0.02$. All other model parameters, except for P_{sh} , are identical to our fiducial models with $P_{\text{sh}} \approx 1$ mbar, including the continuous momentum input at $P = 1$ mbar. We present slice plots in Figure 14 for the two models with $Ri = 0.02$ (*upper* panel) and $Ri = 0.25$ (*lower* panel) at the same times as in Figure 4, i.e., $t/\tau_{\text{cross}} = 0.6, 2, 7, 12$ and 25 . Figures 4 and 14 share the same color-coding scheme.

Similarly to the models with $P_{\text{sh}} = 1$ mbar, the temperature of gas near the shear layer becomes hotter as the kinetic energy of the gas dissipates into heat energy. Then the heat energy spreads out towards regions with relatively low T from the shear layer. Finally, the atmosphere becomes steady. The propagation of the heat energy can be visualized from how K_{zz} at each pressure level evolves over time. This is shown in the *left* panel of Figure 15 for $Ri = 0.02$. This panel shows K_{zz} every $0.1 t/\tau_{\text{cross}}$ for $0 \leq t/\tau_{\text{cross}} \leq 1$ (the dotted lines indicate $t/\tau_{\text{cross}} = 0$ and 1 , while the solid lines mark the intermediate times).

There are two points worth noting: 1) One outcome which has not been seen in the fiducial models, but it is seen in this experiment, is that the regions above the shear layer go through larger increases in T (see high temperatures at $P < 100$ mbar in Figure 14 compared to those at $P > 100$ mbar). This is because a relatively small amount of heat energy is necessary to increase the temperature in a less dense region. 2) Unlike our fiducial models with $P_{\text{sh}} = 1$ mbar, we find that the values of K_{zz} for $Ri = 0.02$ and $Ri = 0.25$ outside the shear layer are comparable when a deeper shear layer is considered. This can be explained from trade-offs between efficiency of heat energy conversion via turbulence and the total kinetic energy budget which can dissipate into heat energy: according to our shear prescription, the total initial momentum (kinetic energy) of the shear layer increases as Ri . Since we do not consider the continuous momentum in-

1024 (high resolution) is 21.8 for $T_{\text{deep}} = 3000 \text{ K}$ and 20.4 for $T_{\text{deep}} = 1800 \text{ K}$.

put near the shear layer in these simulations, the total kinetic energy budget for $Ri = 0.02$ which can dissipate to heat energy is (five times) smaller than that for $Ri = 0.25$. Therefore, even though the heat energy can be converted

via turbulence more efficiently in a more unstable atmosphere with $Ri = 0.02$, however it is limited by the smaller kinetic energy budget contained in the shear layer. On the other hand, for $Ri = 0.25$, the conversion efficiency is lower, but the shear layer has a larger reservoir of kinetic energy.

Overall, a larger heat flux can reach deeper regions when eddy motions are created at larger pressures. In this additional experiment with $P_{\text{sh}} = 100$ mbar, $\tilde{\mathcal{F}}_{\text{H}}$ at $P \simeq 1$ bar (10 bar) becomes comparable to $\sim 0.1\%$ (0.01%) of F_{\star} for both Ri 's; these values are larger than those with $P_{\text{sh}} = 1$ mbar by roughly two orders of magnitude. As a result, as shown in the *right* panel of Figure 15, K_{ZZ} with higher P_{sh} (dotted lines) is larger than that with $P_{\text{sh}} = 1$ mbar (solid lines) by several orders of magnitude throughout the atmosphere, except near $P_{\text{sh}} \simeq 1$ mbar. However, no significant difference in $\tilde{\mathcal{F}}_{\text{H}}$ at $P \simeq 1$ bar is found between the two Ri 's. It is interesting to note that one can recover the dotted lines (higher pressure) by translating towards higher P the lower-pressure (solid) lines by an amount comparable to the ratio between the two P_{sh} values. Note that K_{ZZ} at $P_{\text{sh}} \simeq 1$ mbar is somewhat larger, probably due to the continuous shear motion in the top layers. We will discuss this in more detail in the following section.

These additional results strengthen and broaden our argument that the effect of turbulence on the atmosphere below where eddies form is local, whereas it can cause a spatially large impact on the thermal evolution in the regions above it. Therefore, what is more important for effective heat energy transfer into deeper regions via turbulence is probably where an atmosphere becomes unstable, rather than how unstable it is. Our results further add another aspect, which is that deep shear instabilities can significantly affect the atmosphere above where eddies are created.

5 ANALYTIC RELATIONS FOR P_{SH} AND K_{ZZ}

Based on our results, i.e. the local effect of turbulence, we can now find some useful analytic relations for K_{ZZ} and identify a characteristic minimum pressure of a shear layer at which heat energy created by turbulence can be comparable to the energy necessary to account for the observed radii of hot Jupiters.

Let us consider a shear layer with a height Δz_{sh} , from z_{b} at the bottom to z_{t} at the top of the layer, in an isothermal region of a planet. For simplicity, we assume a constant velocity gradient $dv/dz = \xi = \Delta v_{\text{sh}}/\Delta z_{\text{sh}}$, like the assumption made for our models. Then the shear velocity at z is $v_{\text{sh}}(z) = (\Delta v_{\text{sh}}/\Delta z_{\text{sh}})(z - z_{\text{b}})$. Accordingly, the mean kinetic energy density \bar{E}_{KE} in the shear layer can be estimated as follows,

$$\begin{aligned} \bar{E}_{\text{KE}} &= \frac{1}{2\Delta z_{\text{sh}}} \int_{z_{\text{b}}}^{z_{\text{t}}} \rho(z') v_{\text{sh}}^2(z') dz' \\ &= \frac{1}{2\Delta z_{\text{sh}}} \rho(z = z_{\text{b}}) \xi^2 \int_0^{\Delta z_{\text{sh}}} (z')^2 e^{-\frac{z'}{H}} dz' \\ &= \rho(z = z_{\text{b}}) \xi^2 H^2 \left[\frac{H}{\Delta z_{\text{sh}}} - e^{-\frac{\Delta z_{\text{sh}}}{H}} \left(\frac{H}{\Delta z_{\text{sh}}} + 1 + \frac{\Delta z_{\text{sh}}}{2H} \right) \right], \end{aligned} \quad (18)$$

where we have used an isothermal density profile for $\rho(z)$. We then assume that the kinetic energy in the shear layer is ultimately converted into heat energy via turbulence and is transported downwards at $v_{z,\text{sh}}$, i.e. $\tilde{\mathcal{F}}_{\text{H}} \simeq \bar{E}_{\text{KE}} v_{z,\text{sh}}$. For an energy flux $F_{\text{target}} = fF_{\star} = f\sigma_{\text{SB}}T^4$, with a constant $f \leq 1$, necessary to keep the planet bloated, we find the following relation,

$$\begin{aligned} \rho(z = z_{\text{b}}) (\Delta v_{\text{sh}})^2 v_{z,\text{sh}} &\simeq \frac{F_{\text{target}}}{\left[\frac{H}{\Delta z_{\text{sh}}} - e^{-\frac{\Delta z_{\text{sh}}}{H}} \left(\frac{H}{\Delta z_{\text{sh}}} + 1 + \frac{\Delta z_{\text{sh}}}{2H} \right) \right]} \left(\frac{\Delta z_{\text{sh}}}{H} \right)^2 \\ &\simeq \frac{\beta^2 F_{\text{target}}}{[\beta^{-1} - e^{-\beta}(\beta^{-1} + 1 + 0.5\beta)]}, \end{aligned} \quad (19)$$

where $\beta = \Delta z_{\text{sh}}/H > 0$ and $v_{z,\text{sh}}$ indicates a typical vertical velocity of eddy motions. Strictly speaking, $\rho(z = z_{\text{b}})$ is the density at the bottom of the shear layer and Δv_{sh} is the velocity at the top of the layer (since we assume $v_{\text{sh}}(z = z_{\text{b}}) = 0$), but they can be loosely interpreted as the average location and velocity of the shear layer, simply denoted by $\bar{\rho}_{\text{sh}}$ and \bar{v}_{sh} , respectively. Our simulations suggest that $\beta \simeq 1 - 2$ and $v_{z,\text{sh}}/c_{\text{s}} \simeq \sigma(v_z)/c_{\text{s}} \simeq 10^{-3} - 10^{-4}$ outside the shear layer (see Figure 13), leading to,

$$\bar{\rho}_{\text{sh}} (\bar{v}_{\text{sh}})^2 = \bar{P}_{\text{sh}} \left(\frac{\bar{v}_{\text{sh}}}{c_{\text{s}}} \right)^2 \simeq (10^4 - 10^5) f \sigma_{\text{SB}} T^4 c_{\text{s}}^{-1}. \quad (20)$$

We rewrite this as,

$$\bar{P}_{\text{sh}} \simeq (2 - 35) \text{ bar } (\bar{M}_{\text{sh}})^{-2} \left(\frac{f}{0.01} \right) \left(\frac{T}{3000 \text{ K}} \right)^{7/2}. \quad (21)$$

The above equation implies that, once turbulence is created at $P \simeq$ a few – 35 bar by equatorial jets with $\mathcal{M} \simeq 1$, it can lead to a heat energy transport with an amount as much as 1% of F_{\star} . But this is likely to be a local energy input. For example, in this particular case, since it is still far from the RCB on a level of 1 kbar, a smaller amount of heat energy would be transferred to the RCB. Using this relation, one can find a typical or minimum jet velocity (\bar{M}_{sh}) at any given P (e.g. $P \simeq P_{\text{RCB}}$ or less) and T to achieve F_{target} directly "near" the needed pressure level. The relation between $f = F_{\text{target}}/F_{\star}$ and the jet velocity for different pressure levels above the RCB is visualized in Figure 16. As an example, eddies due to jet streams with $\bar{M}_{\text{sh}} \simeq 0.1$ at $\bar{P}_{\text{sh}} = P_{\text{RCB}} \simeq 1$ kbar (marked with a ' \star ' in the left panel of Figure 16) would generate a heat energy flux of 1% F_{\star} at that pressure level.

Going one step further, we can find an analytic relation for K_{ZZ} . Using Equation 11 (or Equation 20 in Youdin & Mitchell 2010 with $\nabla \simeq 0$) with $F_{\text{H}} \simeq \bar{\rho}_{\text{sh}} \bar{v}_{\text{sh}}^2 \sigma(v_{z,\text{sh}})$, we find that,

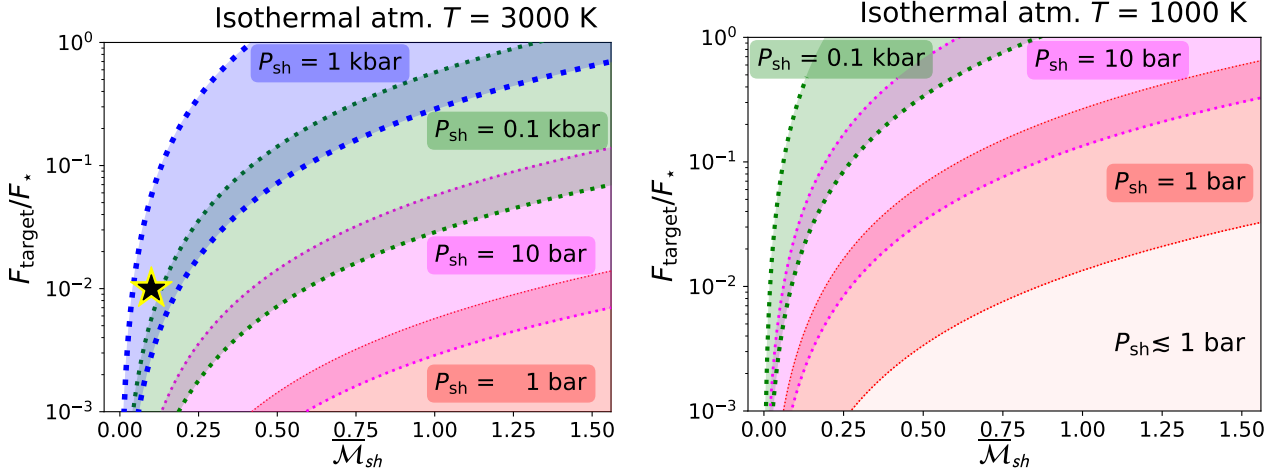


Figure 16. Local shear-driven heat energy flux F_{target} with respect to the incoming stellar flux F_{\star} , in isothermal atmospheres with $T = 3000$ K (left panel) and $T = 1000$ K (right panel) as a function of jet stream velocity (\mathcal{M}_{sh}) at different pressure levels. The flux ratio $F_{\text{target}}/F_{\star}$ is estimated using Equation (21), hence appearing as a region at a given P . The darker zones between regions indicate where two zones overlap. The dotted lines demarcating the boundary of each region correspond to the upper and lower limits of the flux ratio at that pressure level. The lines become thicker as P increases (\searrow direction). Note that, for the cases considered in our simulations, i.e. $P_{\text{sh}} = 1$ mbar and 100 mbar, the ratio $F_{\text{target}}/F_{\star}$ is smaller than 10^{-3} . The star in the left panel indicates a jet stream velocity which would generate a heat flux of 1% F_{\star} near the RCB.

$$\begin{aligned}
 K_{\text{ZZ}} &\simeq \frac{\bar{\rho}_{\text{sh}} \bar{v}_{\text{sh}}^2 \sigma(v_{\text{z,sh}})}{\bar{\rho}_{\text{sh}} g} \simeq \frac{(\bar{v}_{\text{sh}})^2 \sigma(v_{\text{z,sh}})}{g} \\
 &\simeq 4 (\bar{v}_{\text{sh}})^2 \left(\frac{\sigma(v_{\text{z,sh}})}{10^{-2} c_s} \right) \left(\frac{1000 \text{ cm s}^{-2}}{g} \right) \\
 &\propto (\bar{v}_{\text{sh}})^2.
 \end{aligned} \tag{22}$$

From this, we can see that the important factor in determining K_{ZZ} at the shear layer is probably $(\bar{v}_{\text{sh}})^2$, or the specific kinetic energy of eddy motions. Outside the shear layer, K_{ZZ} would extend following the power law of $P^{-1.2}$ (see Equation 17). This also explains why we find similar K_{ZZ} at different \bar{P}_{sh} , as we briefly mentioned in §4.2, since we always assume $\bar{v}_{\text{sh}} \simeq c_s$, $K_{\text{ZZ}} \simeq (10^{11} - 10^{12}) \text{ cm}^2 \text{ s}^{-1}$ at $T = 3000$ K at \bar{P}_{sh} . However, the location of the shear layer (\bar{P}_{sh}) is also important for the amount of heat flux transported, since $\tilde{\mathcal{F}}_{\text{H}} \propto \rho(\bar{P}_{\text{sh}}) K_{\text{ZZ}}$, i.e. there is a direct dependence on the (location-dependent) kinetic energy, rather than simply on the specific kinetic energy.

To summarize, we suggest that the key factors in determining $\tilde{\mathcal{F}}_{\text{H}}$ and K_{ZZ} are the kinetic energy and the specific kinetic energy at the shear layer, respectively.

6 CAVEATS

Our suite of hydrodynamics simulations, modelling turbulence and shocks in the atmospheres of hot Jupiters, show that their effects on the transport of heat energy fluxes are local in space and transient in time. As we discussed in §4.1, our results for the effects of turbulence and shocks are reasonably robust. However, in the following we point out two caveats which will require future investigation.

(i) Radiative effects

It has been shown in global circulation models that shear

motions at different pressure levels are triggered by east-west stream motions as the day side gets irradiated more than the night side. Furthermore, as mentioned above, the location of the RCB is closely related to where the radiative heating and cooling are balanced. All of this implies that the evolution of the planet atmospheres is governed by complicated physics of radiation, cooling and hydrodynamics.

In our study, we mimic the shear forcing by considering a momentum source. This allows us to better focus on the hydrodynamical effects of turbulence but we may miss some of the impact of radiative transfer and cooling. For example, it is possible that radiative transfer may be smoothing out some of the temperature gradients near the optically thin regions seen in our simulations (e.g. Figures 4 and 14). The radiative time scale near $P \simeq 1 - 100$ mbar (e.g., $\sim 10^3 - 10^4$ s in Figure 4 of Showman & Guillot 2002) can be comparable to the eddy evolution timescale in our simulations. That means that in some cases the cooling could produce non-negligible effects on the dynamics of the atmosphere. This will be investigated in future studies.

(ii) Vertical location of RCB, P_{RCB}

The internal entropy is an important parameter for the vertical location of the radiative-convective boundary, or P_{RCB} . In general, P_{RCB} increases with the internal entropy. In this study, we only assume the same internal entropy in all of our atmospheric models. Hence it is not straightforward to quantify the heat flux or K_{ZZ} directly from our results, for atmospheres with initially different P_{RCB} . As a qualitative assessment based on the small effective spatial range of turbulence ($\sim 2H$) and the rapidly decreasing heat flux outside that range, it is likely that the magnitude of the heat flux penetrating into the RCB would be insignificant, unless turbulence occurred sufficiently close to the RCB. However, considering the power-law tail of K_{ZZ} shown in Figure 10 extending to higher P , for planets with higher entropy (lower P_{RCB}) and with long-lived or continuously created turbu-

lence in less dense regions, we can still consider the cumulative effects of small, but continuous heat energy supplies into deep regions.

7 SUMMARY AND FUTURE DIRECTION

We have performed 3-dimensional hydrodynamics simulations to investigate the effects of shock and turbulence on energy penetration into hot Jupiter atmospheres, under a variety of shear gradients. We find that the effects of turbulence on the kinetic and heat energy transfer are local, generally within a spatial range of $z \sim 2H$, below the shear layer. However, turbulence can drive a spatially and thermally great influence on in the regions above it. The temperature increases most significantly near the shear layer due to turbulence, which can further enhance the temperature inversion, in addition to the other effects already discussed in the literature (Showman et al. 2008; Rauscher & Menou 2010). We also find that shock formation is insignificant. The time-averaged heat energy flux at $P \sim 1$ bar when the atmosphere becomes steady is on the order of 0.001% of F_\star with a shear motion at the top of the atmosphere ($P_{\text{sh}} \approx 1$ mbar) and 0.1% with a deeper shear layer at $P_{\text{sh}} \approx 100$ mbar. Accordingly, K_{zz} is higher for the deeper shear layer. Therefore, our results suggest that turbulence near less dense regions ($P \gtrsim 1$ mbar) does not lead to transport of heat energy deep enough to explain the inflated radii of hot Jupiters, regardless of how violent the turbulence is. On the other hand, as eddy motions occur at deeper regions ($P \gtrsim 100$ mbar), it is more likely that the heat energy is transferred more effectively throughout the atmosphere (upwards and downwards) due to relatively large kinetic energy budgets. Therefore, it is more important how deep turbulence occurs in the atmosphere (or, P_{sh}), than how unstable the atmosphere is (or, Ri) for effective transfer of energy.

Understanding the role of turbulence itself is a crucial step prior to modelling global-scale atmospheres. Future work will aim at modeling global circulation of hot Jupiters including radiation.

ACKNOWLEDGEMENTS

We are grateful to Kevin Heng and Andrew Youdin for their constructive feedbacks. We also thank the anonymous referee for constructive comments and suggestions which helped us to improve the paper. The authors acknowledge the analysis toolkit `yt` (Turk et al. 2011) and `matplotlib` (Hunter 2007) for making the plots in the paper. The authors would like to thank Stony Brook Research Computing and Cyberinfrastructure, and the Institute for Advanced Computational Science at Stony Brook University for access to the high-performance SeaWulf computing system, which was made possible by a \$1.4M National Science Foundation grant (#1531492). MZ was supported by DOE/Office of Nuclear Physics grant DE-FG02-87ER40317 for development of Castro. Castro is freely available at <https://github.com/AMReX-Astro/Castro>. The simulations used the `planet` setup in the code repository.

REFERENCES

- Almgren A. S., Bell J. B., Nonaka A., Zingale M., 2008, *ApJ*, **684**, 449
- Almgren A. S., et al., 2010, *ApJ*, **715**, 1221
- Batygin K., Stevenson D. J., 2010, *ApJL*, **714**, L238
- Bodenheimer P., Lin D. N. C., Mardling R. A., 2001, *ApJ*, **548**, 466
- Burrows A., Hubeny I., Budaj J., Hubbard W. B., 2007, *ApJ*, **661**, 502
- Chandrasekhar S., 1961, Hydrodynamic and hydromagnetic stability
- Colella P., 1990, *Journal of Computational Physics*, **87**, 171
- Colella P., Woodward P. R., 1984, *Journal of Computational Physics*, **54**, 174
- Dobbs-Dixon I., Agol E., 2013, *M.N.R.A.S.*, **435**, 3159
- Fromang S., Leconte J., Heng K., 2016, *A&A*, **591**, A144
- Guillot T., Showman A. P., 2002, *A&A*, **385**, 156
- Hannoun I. A., Fernando H. J. S., List E. J., 1988, *Journal of Fluid Mechanics*, **189**, 189
- Heng K., 2012, *ApJL*, **761**, L1
- Heng K., Showman A. P., 2015, *Annual Review of Earth and Planetary Sciences*, **43**, 509
- Heng K., Menou K., Phillipps P. J., 2011a, *M.N.R.A.S.*, **413**, 2380
- Heng K., Frierson D. M. W., Phillipps P. J., 2011b, *M.N.R.A.S.*, **418**, 2669
- Howard A. W., et al., 2012, *ApJ Supp.*, **201**, 15
- Hunter J. D., 2007, *Computing In Science & Engineering*, **9**, 90
- Hurlburt N. E., Toomre J., Massaguer J. M., 1984, *ApJ*, **282**, 557
- Ibgui L., Burrows A., 2009, *ApJ*, **700**, 1921
- Ibgui L., Spiegel D. S., Burrows A., 2011, *ApJ*, **727**, 75
- Izakov M. N., 2001, *Planet. Space Sci.*, **49**, 47
- Izakov M. N., 2002, *Solar System Research*, **36**, 193
- Jackson B., Greenberg R., Barnes R., 2008, *ApJ*, **681**, 1631
- Komacek T. D., Youdin A. N., 2017, *ApJ*, **844**, 94
- Li J., Goodman J., 2010, *ApJ*, **725**, 1146
- Nonaka A., Almgren A. S., Bell J. B., Lijewski M. J., Malone C. M., Zingale M., 2010, *ApJ Supp.*, **188**, 358
- Nonaka A., Aspden A. J., Zingale M., Almgren A. S., Bell J. B., Woosley S. E., 2012, *ApJ*, **745**, 73
- Perna R., Menou K., Rauscher E., 2010a, *ApJ*, **719**, 1421
- Perna R., Menou K., Rauscher E., 2010b, *ApJ*, **724**, 313
- Perna R., Heng K., Pont F., 2012, *ApJ*, **751**, 59
- Rauscher E., Menou K., 2010, *ApJ*, **714**, 1334
- Rauscher E., Menou K., 2012, *ApJ*, **745**, 78
- Showman A. P., Guillot T., 2002, *A&A*, **385**, 166
- Showman A. P., Cooper C. S., Fortney J. J., Marley M. S., 2008, *ApJ*, **682**, 559
- Showman A. P., Fortney J. J., Lian Y., Marley M. S., Freedman R. S., Knutson H. A., Charbonneau D., 2009, *ApJ*, **699**, 564
- Spiegel D. S., Silverio K., Burrows A., 2009, *ApJ*, **699**, 1487
- Turk M. J., Smith B. D., Oishi J. S., Skory S., Skillman S. W., Abel T., Norman M. L., 2011, *ApJ Supp.*, **192**, 9
- Wang J., Fischer D. A., Horch E. P., Huang X., 2015, *ApJ*, **799**, 229
- Youdin A. N., Mitchell J. L., 2010, *ApJ*, **721**, 1113
- Zingale M., et al., 2002, *ApJ Supp.*, **143**, 539
- Zingale M., Almgren A. S., Bell J. B., Nonaka A., Woosley S. E., 2009, *ApJ*, **704**, 196
- Zingale M., Nonaka A., Almgren A. S., Bell J. B., Malone C. M., Woosley S. E., 2011, *ApJ*, **740**, 8

This paper has been typeset from a $\text{\TeX}/\text{\LaTeX}$ file prepared by the author.